

Gliese 12 b, A Temperate Earth-sized Planet at 12 Parsecs Discovered with *TESS* and *CHEOPS*

Shishir Dholakia,^{1*} † Larissa Palethorpe,^{2,3,4*} ‡ Alexander Venner,¹ Annelies Mortier,⁵ Thomas G. Wilson,^{6,7} Chelsea X. Huang,¹ Ken Rice,^{2,3} Vincent Van Eylen,⁴ Emma Nabbie,¹ Ryan Cloutier,¹² Walter Boschin,^{8,9,10} David Ciardi,¹¹ Laetitia Delrez,^{13,14,15} Georgina Dransfield,⁵ Elsa Ducrot,¹⁶ Zahra Essack,¹⁷ Mark E. Everett,¹⁸ Michaël Gillon,¹⁹ Matthew J. Hooton,²⁰ Michelle Kunitomo,^{21,22} David W. Latham,²³ Mercedes López-Morales,²³ Bin Li,²⁴ Fan Li,²⁴ Scott McDermott,²⁵ Simon Murphy,¹ Catriona A. Murray,²⁶ Sara Seager,^{21,27,28} Mathilde Timmermans,¹³ Amaury Triaud,⁵ Daisy A. Turner,⁵ Joseph D. Twicken,²⁴ Andrew Vanderburg,²¹ Su Wang,²⁴ Robert A. Wittenmyer,¹ and Duncan Wright¹
(Affiliations can be found after the references)

Accepted 2024 April 29. Received 2024 April 29; in original form 2024 January 30

ABSTRACT

We report on the discovery of Gliese 12 b, the nearest transiting temperate, Earth-sized planet found to date. Gliese 12 is a bright ($V = 12.6$ mag, $K = 7.8$ mag) metal-poor M4V star only 12.162 ± 0.005 pc away from the Solar System with one of the lowest stellar activity levels known for an M-dwarf. A planet candidate was detected by *TESS* based on only 3 transits in sectors 42, 43, and 57, with an ambiguity in the orbital period due to observational gaps. We performed follow-up transit observations with *CHEOPS* and ground-based photometry with MINERVA-Australis, SPECULOOS, and Purple Mountain Observatory, as well as further *TESS* observations in sector 70. We statistically validate Gliese 12 b as a planet with an orbital period of 12.76144 ± 0.00006 days and a radius of $1.0 \pm 0.1 R_{\oplus}$, resulting in an equilibrium temperature of ~ 315 K. Gliese 12 b has excellent future prospects for precise mass measurement, which may inform how planetary internal structure is affected by the stellar compositional environment. Gliese 12 b also represents one of the best targets to study whether Earth-like planets orbiting cool stars can retain their atmospheres, a crucial step to advance our understanding of habitability on Earth and across the Galaxy.

Key words: exoplanets – planets and satellites: detection – planets and satellites: terrestrial planets – techniques: photometric – stars: individual: Gliese 12 – planets and satellites: individual: Gliese 12 b

1 INTRODUCTION

Our knowledge of terrestrial planets akin to Earth around stars beyond our own has progressed vastly since the beginning of the 2010s. The *Kepler* mission revealed that these small planets are abundant around low-mass M-dwarf stars (Dressing & Charbonneau 2015; Muirhead et al. 2015). This discovery has opened the doors to a wealth of study on small planets orbiting M dwarfs throughout the last decade. M dwarfs are especially well-suited for transiting planet detection and characterisation due to their frequency in our galaxy, small size, and low luminosities. These properties of M dwarfs result in advantages in detection efficiency due to nearer transiting systems, deeper transits,

and higher *a priori* geometric transit probability for temperate planets due to their closer orbital separations.

A key uncertainty in our current knowledge of these planets is whether they can retain their atmospheres, a prerequisite for their habitability (Seager & Deming 2010). The recently-launched James Webb Space Telescope (*JWST*; Gardner et al. 2006) is capable of detecting atmospheric features of such planets with transmission and emission spectroscopy, should they exist (Rieke et al. 2015). However, *JWST* has so far observed featureless spectra for these planets (Lustig-Yaeger et al. 2023; Lim et al. 2023; May et al. 2023; Zieba et al. 2023). Though these null detections may intriguingly suggest that these planets lack atmospheres, their interpretation is complicated by signal-to-noise limitations and higher than anticipated effects of stellar contamination. Expanding the catalogue of terrestrial planets orbiting bright, nearby M dwarfs will be crucial for resolving this uncertainty.

The NASA Transiting Exoplanet Survey Satellite (*TESS*; Ricker et al. 2014) is performing an ongoing survey for transiting exoplanets

* These two authors contributed equally to this work & should be considered joint first authors.

† E-mail: dholakia.shishir@gmail.com

‡ E-mail: larissa.palethorpe@ed.ac.uk

across much of the sky. In contrast to the long-duration, deep-and-narrow observing strategy of *Kepler*, *TESS* observes a much larger 2300 deg² area of the sky using its four refractive 10 cm CCD cameras, with sky coverage divided in time into “sectors” with durations of 27.4 days. This means that *TESS* is sensitive to short-period planets orbiting bright stars. Furthermore, the red-optimised 600-1000 nm *TESS* bandpass increases its photometric sensitivity for cool stars such as M dwarfs (Ricker et al. 2014).

TESS has discovered a significant number of small exoplanets orbiting M dwarfs throughout both its two-year prime mission and subsequent extended mission (e.g. Vanderspek et al. 2019; Luque et al. 2019; Günther et al. 2019; Kostov et al. 2019; Winters et al. 2019; Cloutier et al. 2020, 2021; Shporer et al. 2020; Gan et al. 2020; Gilbert et al. 2020, 2023; Trifonov et al. 2021; Burt et al. 2021; Silverstein et al. 2022). *TESS* detections have demonstrated that terrestrial planets are common around the nearest M dwarfs (Ment & Charbonneau 2023), though the number of these planets detected around mid-late M dwarfs ($<0.3 R_{\odot}$) is lower than anticipated (Benz & Bean 2022). Now in its sixth year of operations, *TESS* continues to extend its observational baseline as it re-observes much of the sky. This enables the discovery of new exoplanets with longer orbital periods and, hence, lower equilibrium temperatures.

The Characterising ExOPlanets Satellite (*CHEOPS*; Benz et al. 2021) has found great success in taking precise transit photometry and determining accurate planetary parameters of *TESS* discoveries that enables further characterisation by *JWST* and other instruments (Lacedelli et al. 2022; Tuson et al. 2023; Wilson et al. 2022; Fairington et al. 2024; Palethorpe et al. 2024). *CHEOPS* utilises a 30 cm telescope to perform high precision, targeted photometry in order to refine transit ephemerides, ascertain orbital periods, and improve on the radius precision of planets detected by *TESS* and other transit surveys (Benz et al. 2021), as well discovering new planets. The larger aperture of *CHEOPS* compared to *TESS* also provides high signal-to-noise transits that may be challenging or impossible to obtain from the ground. Due to *TESS*’s scanning strategy, transits of longer period exoplanets are often missed, rendering the orbital period ambiguous. Follow-up observations by *CHEOPS* can ascertain the orbital periods of these planets. A network of ground-based photometers and spectrographs also complements *CHEOPS* in targeting *TESS* Objects of Interest (TOIs) in order to confirm, validate, and refine the characteristics of the systems.

In this work we present the discovery of a temperate ($F = 1.6 \pm 0.2 S_{\oplus}$) Earth-sized ($R_b = 1.0 \pm 0.1 R_{\oplus}$) planet orbiting the M-dwarf Gliese 12 found and validated through *TESS* and *CHEOPS* observations. Gliese 12 is bright ($V = 12.6$ mag, $K = 7.8$ mag), nearby (12.162 ± 0.005 pc), and is characterised by low magnetic activity; these factors establish Gliese 12 b as a prime target for further characterisation, such as mass measurement via RV observations and atmospheric study through transmission spectroscopy.

We organise this work as follows: In Section 2, we detail the space- and ground-based photometry, spectroscopy, and imaging data for this target. In Section 3, we compile and derive the properties of Gliese 12. Section 4 enumerates and precludes the possible scenarios of a false positive exoplanet detection with the available data, validating Gliese 12 b as a genuine exoplanet. We then describe our approach to modelling the transits of Gliese 12 b from the available data in Section 5. In Section 6, we comment on Gliese 12 b’s prospects for further study, including future mass measurement, atmospheric characterisation, and this target’s utility to exoplanet demography. Finally, in Section 7, we summarise and conclude the work.

2 OBSERVATIONS

2.1 Photometry

2.1.1 *TESS*

Gliese 12 (TIC 52005579, TOI-6251) was first observed by *TESS* during ecliptic plane observations in sectors 42 and 43 of year 4 in its first extended mission (Ricker et al. 2014; Ricker 2021), between 2021 August 21 – 2021 October 11 (BJD 2459447.19 – BJD 2459498.39). It was then re-observed during sector 57 of year 5 in the second *TESS* extended mission between 2022 September 30 – 2022 October 29 (BJD 2459852.85 – BJD 2459881.62). Over a total of 82.2 days, *TESS* observations of Gliese 12 were combined into 20s cadence target pixel frames¹. The data observed in sector 42 were taken on CCD 2 of camera 2, whilst the data observed in sectors 43 and 57 were taken on CCD 3 of camera 1.

The data were processed in the *TESS* Science Processing Operations Center (SPOC; Jenkins et al. (2016)) pipeline at NASA Ames Research Center. The SPOC conducted a transit search of the *TESS* data up to sector 57 on 2023 February 04 with an adaptive, noise-compensating matched filter (Jenkins 2002; Jenkins et al. 2010, 2020). The search identified a Threshold Crossing Event (TCE) with 12.76148 d period. The TCE was reported with a Multiple Event Statistic (MES) S/N statistic of 8.0, above the lower limit of 7.1 required for a TCE to undergo further vetting. An initial limb-darkened transit model was fitted (Li et al. 2019) and a suite of diagnostic tests were conducted to help assess the planetary nature of the signal (Twicken et al. 2018). The transit depth associated with the TCE was 1180 ± 173 ppm. Inspection of the SPOC Data Validation (DV) report reveals two possible periods for the transit signal, either 12.76 d or a factor of two larger (25.52 d), due to gaps in the photometry coincident with alternating transits.

TESS photometry in sectors 42 and 43 was strongly affected by crossings of the Earth and Moon in the field of view (Fausnaugh et al. 2021a,b). As a result observations of Gliese 12 in both sectors contain large mid-sector gaps, 7.6 d between BJD 2459453.64 – BJD 2459461.24 in sector 42 and 5.1 d between BJD 2459482.11 – BJD 2459487.19 in sector 43 (Figure 1), and there is likewise a large observing gap between the two sectors. The phasing of these gaps means that only one transit of the Gliese 12 planet candidate (BJD 2459497.18) was observed, with up to 3 transits falling outside of active observation. During sector 57 *TESS* entered safe mode for 3.13 days between BJD 2459863.28 – BJD 2459866.41; there are also three smaller gaps for data downlinks between BJD 2459860.58 – BJD 2459860.80, BJD 2459867.25 – BJD 2459867.47, and BJD 2459874.61 – BJD 2459874.82, spanning a total of 0.63 d (Fausnaugh et al. 2022). Two transits were successfully observed towards the beginning and end of sector 57 (BJD 2459854.51 and BJD 2459880.03), however the location of a possible transit at BJD 2459867.27 falls into the data gap caused by the second data downlink.

The incidence of these data gaps, visualised in Figure 1, caused the initial ambiguity in the orbital period between 12.76 d or 25.52 d. Despite this uncertainty, the TCE passed an initial triage with the *TESS*-ExoClass (TEC) classification algorithm² and was subsequently vet-

¹ This star has been observed by *TESS* as part of Guest Investigator programs G04033 (PI: Winters), G04148 (PI: Robertson), G04191 (PI: Burt), G04211 (PI: Marocco), and G04214 (PI: Cloutier) in year 4; programs G05087 (PI: Winters), G05109 (PI: Marocco), and G05152 (PI: Cloutier) in year 5; and program G06131 (PI: Shporer) in year 6.

² <https://github.com/christopherburke/TESS-ExoClass>

ted by the *TESS* team. The TCE was then duly promoted to *TESS* Object of Interest (TOI; Guerrero et al. (2021)) planet candidate status and alerted as TOI-6251.01 on 2023 April 03. The TOI was alerted with the 25.52 d period, but a note was included on the factor-of-two orbital period ambiguity.

TESS observed Gliese 12 again in sector 70, during its second ecliptic plane survey in year 6. Observations were captured with a 120s cadence on CCD 3 of camera 2 between 2023 September 20 – 2023 October 16 (BJD 2460208.79 – BJD 2460232.97). The *TESS* sector 70 photometry covers two consecutive transits of TOI-6251.01 (also known as Gliese 12 b) separated by 12.76 d, confirming the short-period orbital solution.

For the photometric analysis, we download the *TESS* photometry from the Mikulski Archive for Space Telescopes (MAST)³ and use the Presearch Data Conditioning Simple Aperture Photometry (PD-CSAP; Stumpe et al. (2012, 2014); Smith et al. (2012)) light curve reduced by the SPOC. We use the quality flags provided by the SPOC pipeline to filter out poor quality data.

2.1.2 CHEOPS

To confirm and characterise the planet in the Gliese 12 system we obtained five visits covering transits of planet b with the *CHEOPS* spacecraft (Benz et al. 2021) through the *CHEOPS* AO-4 Guest Observers programmes with ID:07 (PI: Palethorpe) and ID:12 (PI: Verner). The observation log for our *CHEOPS* observations is presented in Table 1.

The data were processed using the *CHEOPS* Data Reduction Pipeline (DRP 14.1.3; Hoyer et al. 2020) that conducts frame calibration, instrumental and environmental correction, and aperture photometry using a pre-defined range of radii ($R = 15\text{--}40''$). For all visits of Gliese 12 we selected the DEFAULT aperture, which has a radius of 25 pixels. The DRP produced flux contamination (see Hoyer et al. 2020 and Wilson et al. 2022 for computation and usage) that was subtracted from the light curves. We retrieved the data and corresponding instrumental bases vectors, assessed the quality using the *pycheops* Python package (Maxted et al. 2022), and decorrelated with the parameters suggested by this package, which can be found in Table 1. Outliers were also trimmed from the light curves, with points that were 4σ away from the median value removed. We then used these detrended data for further analysis. Table 3 shows which of the possible periods the various *CHEOPS* transits cover, whilst three of the transits observed occurred when both a 12.76d and 25.5d period were possible, a further two transits were observed when only a 12.76d period was possible, confirming this as the orbital period of Gliese 12 b.

2.1.3 MINERVA-Australis

We used three telescopes of the MINERVA-Australis array (Addison et al. 2019) in clear bands to simultaneously observe a full transit of Gliese 12 b on the night of 2023 September 11. Telescopes 1 and 2 are both equipped with ZWO1600 CMOS cameras, each with a field of view of $27' \times 18'$, and plate scale of 0.67 arc-second per pixel. Telescope 3 is equipped with ZWO295 CMOS camera, with a field of view of $21' \times 14'$, and a plate scale of 0.3 arc-second per pixel. We used exposure durations of 30 seconds for Telescope 1 and 2 and 60 seconds for telescope 3. We used *astroImageJ* (Collins et al. 2017) to extract the light curves. The aperture radii are $\sim 8.7''$ for all three

telescopes. The observation of telescope 3 was interrupted during the transit event, therefore did not achieve the necessary precision for the independent detection of the transit. Thus, we do not include data from telescope 3 for our global analysis. We detrend using the x and y positions, airmass and quadratic time series terms. A log of these observations and decorrelations can be found in Table 2, and the possible period of the transiting planet covered by these observations can be found in Table 3.

2.1.4 SPECULOOS

We observed two transits of Gliese 12 b with the SPECULOOS Southern Observatory (SSO; Jehin et al. 2018; Sebastian et al. 2021; Gillon 2018; Murray et al. 2020; Delrez et al. 2018). SSO is composed of four 1m-class telescopes named after the Galilean moons (Io, Europa, Ganymede and Callisto), it is located at ESO Cerro Paranal Observatory in Chile. The telescopes are identical, each equipped with a 2K \times 2K Andor CCD camera with a pixel scale of $0.35''$ per pixel, resulting in a field of view of $12' \times 12'$. We obtained a transit of Gliese 12 b on 2023 September 23 with Europa with 10s exposures in the *Sloan-r'* filter, totalling 1213 measurements. A second transit was obtained simultaneously with Io, Europa and Ganymede on the 2023 November 26, also with 10s exposures in the *Sloan-r'* filter. These observations represent 754, 741, and 751 measurements, respectively. All the data analysis was done using a custom pipeline built with the *prose*⁴ package (Garcia et al. 2022, 2021). We performed differential photometry and the optimum apertures were $3.26''$, $3.45''$, $3.23''$, and $3.17''$ respectively for the Europa observation on the night of the 2023 September 23, and the Io, Europa, and Ganymede observations on the night of 2023 November 26. A log of these observations and their decorrelation parameters can be found in Table 2, and the possible period of the transiting planet covered by these observations can be found in Table 3.

2.1.5 Purple Mountain Observatory

We observed one transit with Purple Mountain Observatory (PMO) on the night of 2023 September 01. The telescope is an 80 cm azimuthal-mounting high precision telescope at Purple Mountain Observatory Yaoan Station in Yunnan Province, in the southwest of China. The telescope's field of view is 11.8 arcmin. It is a Ritchey-Chretien telescope with a 2048 \times 2048 pixel PI CCD camera. The spatial resolution for each axis is 0.347 arcsec per pixel. We used the Ic broadband filter for the observation. The cadence of the observations was 55 seconds and the exposure time was 50 seconds. A log of these observations and their decorrelation parameters can be found in Table 2, and the possible period of the transiting planet covered by these observations can be found in Table 3.

2.2 Spectroscopy

2.2.1 TRES

We obtained an additional 4 observations of Gliese 12 via the Tillinghast Reflector Echelle Spectrograph (TRES; Fűrész et al. (2008)) on the 1.5m reflector at the Fred Lawrence Whipple Observatory in Arizona, USA. TRES is a fiber-fed echelle spectrograph with a spectral resolution of 44,000 over the wavelength range of 390–910nm. The

³ <https://archive.stsci.edu/tess>

⁴ <https://github.com/lgrcia/prose>

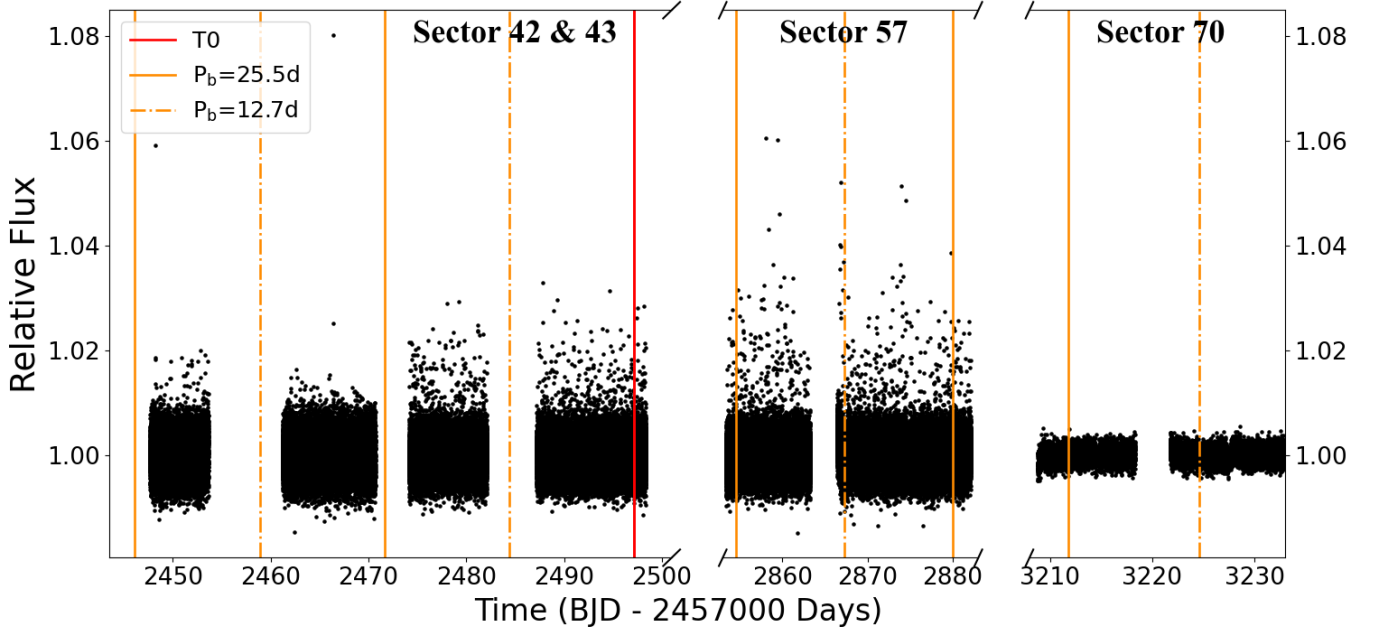


Figure 1. *TESS* photometry of Gliese 12. Figure shows the 20s cadence PDCSAP light curve for sectors 42, 43 & 57 and the 120s cadence PDCSAP light curve for sector 70, where systematic errors have been removed, but the resulting light curve has not been corrected for low-frequency variations such as stellar activity. Over-plotted are the possible periods of the transiting planet, where the red solid line shows the transit centre, the orange dashed-dotted lines shows times consistent with a 12.76d and 25.52d period, and the solid orange line shows times consistent with only a 12.76d period.

Table 1. Log of *CHEOPS* Observations of Gliese 12 b. The column T_{exp} gives the exposure time in terms of the integration time per image multiplied by the number of images stacked on-board prior to download. N_{obs} is the number of frames. Effic. is the proportion of the time in which unobstructed observations of the target occurred. R_{ap} is the aperture radius used for the photometric extraction. RMS is the standard deviation of the residuals from the best fit after the DRP has been applied. The variables in the final column are as follows: time, t ; spacecraft roll angle, ϕ ; PSF centroid position, (x, y) ; smear correction, smear ; aperture contamination, contam ; image background level, bg .

Start Date (UTC)	Duration (h)	T_{exp} (s)	N_{obs}	Effic. (%)	File key	APER	R_{ap} (pixels)	RMS (ppm)	Decorrelation
2023-09-24T00:04	11.41	60	513	74.9	CH_PR240007_TG000101_V0300	DEFAULT	25	801	$\sin(\phi), \cos(\phi), \text{contam}, \text{smear}, \text{bg}$
2023-10-06T18:20	12.76	60	481	62.8	CH_PR240007_TG000102_V0300	DEFAULT	25	846	$t, t^2, x, x^2, y, y^2, \sin(\phi), \sin(2\phi), \cos(\phi), \cos(2\phi), \text{contam}, \text{smear}, \text{bg}$
2023-10-19T16:33	6.80	60	222	54.3	CH_PR240012_TG000701_V0300	DEFAULT	25	752	$t^2, \text{contam}, \text{smear}, \text{bg}$
2023-11-14T06:30	6.92	60	241	57.9	CH_PR240012_TG000702_V0300	DEFAULT	25	910	$t, x, y, \sin(\phi), \cos(\phi), \text{bg}$
2023-11-27T18:35	7.44	60	248	55.5	CH_PR240012_TG000101_V0300	DEFAULT	25	1114	$t, x, y, \sin(\phi), \cos(\phi), \text{bg}$

observations were taken between 2016 October 13 – 2021 September 11 as part of the M-dwarf survey of [Winters et al. \(2021\)](#), using the standard observing procedure of obtaining a set of three science observations surrounded by ThAr calibration spectra. The science spectra were then combined to remove cosmic rays and wavelength calibrated using the ThAr spectra, with the extraction technique following procedures outlined in [Buchhave et al. \(2010\)](#). The spectra had signal-to-noise ratios in the range 20–24 (average SNR = 21) at $\sim 716\text{nm}$ and are presented in [Table A1](#).

2.2.2 HARPS-N

We obtained 13 spectra for Gliese 12 with the HARPS-N spectrograph ($R = 115000$) ([Cosentino et al. 2012](#)) installed on the 3.6m Telescopio Nazionale Galileo (TNG) at the Observatorio de los Muchachos in La Palma, Spain. These observations were taken between 2023 August 09 – 2023 October 01 (BJD 2460165.66 – BJD 2460218.56) as part of the HARPS-N Collaboration’s Guaranteed Time Observations (GTO) programme. The observational strategy consisted of exposure times of 1800s per observation. We obtained spectra with signal-to-noise ratios in the range 12–35 (average SNR = 25) at 550nm.

The spectra were reduced with 2 different methods. The first used

Table 2. Log of ground-based photometric observations of Gliese 12 b. The column T_{exp} gives the exposure time in terms of the integration time per image multiplied by the number of images stacked on-board prior to download. N_{obs} is the number of frames. The variables in the final column are as follows: time, t ; position of the target star on the CCD (x, y), and the FWHM of the PSF.

Start Date (UTC)	Duration (h)	T_{exp} (s)	N_{obs}	Observatory/Telescope	Decorrelation
2023-09-11T11:39	3.852	30.0	197	MINERVA T1	$t, x, y, \text{airmass}$
2023-09-11T11:39	3.852	60.0	266	MINERVA T2	$t, x, y, \text{airmass}$
2023-09-24T01:30	7.019	10.0	1207	SPECULOOS Europa	t^2, x^2
2023-11-01T13:01	3.000	55.0	210	PMO	x, y, FWHM
2023-11-27T00:01	4.251	10.0	754	SPECULOOS Io	$\text{airmass}, \text{FWHM}$
2023-11-27T00:02	4.234	10.0	741	SPECULOOS Europa	t
2023-11-27T00:02	4.239	10.0	751	SPECULOOS Ganymede	t

Table 3. Log of photometric observations of Gliese 12 b relative to the possible period of the transiting planet. The Period column relates to the period ambiguity surrounding Gliese 12 b, where T_0 refers to the transit centre time of BJD 2459497.185, P_1 refers to the possible 12.76d period, and P_2 refers to the possible 25.5d period.

Date (UTC)	Observatory/Telescope	Period
2023-09-11	MINERVA (T1, T2)	$T_0 + 55 P_1$
2023-09-24	CHEOPS	$T_0 + 56 P_1$ or $T_0 + 28 P_2$
2023-09-24	SPECULOOS (Europa)	$T_0 + 56 P_1$ or $T_0 + 28 P_2$
2023-10-06	CHEOPS	$T_0 + 57 P_1$
2023-10-19	CHEOPS	$T_0 + 58 P_1$ or $T_0 + 29 P_2$
2023-11-01	PMO	$T_0 + 59 P_1$
2023-11-14	CHEOPS	$T_0 + 60 P_1$ or $T_0 + 30 P_2$
2023-11-27	CHEOPS	$T_0 + 61 P_1$
2023-11-27	SPECULOOS (Europa, Ganymede, Io)	$T_0 + 61 P_1$

version 2.3.5 of the HARPS-N Data Reduction Software (DRS) (Dumusque et al. 2021), with a M4 mask used in the cross-correlation function (CCF), resulting in an RV RMS of 2.60 ms^{-1} and RV precision of 2.95 ms^{-1} . The second method used was the line-by-line (LBL) method (Artigau et al. 2022). The LBL code⁵ performs a simple telluric correction by fitting a TAPAS model (Bertaux et al. 2014), and has been shown to significantly improve the RV precision of M dwarfs observed with optical RV spectrographs (Cloutier et al. 2024). The LBL method resulted in an average RV RMS of 2.69 ms^{-1} , which is similar to that of the CCF method, however the average RV precision significantly improved to 1.15 ms^{-1} .

The HARPS-N data are presented in Table A2, which includes the radial velocities as well as the activity indicators: full width at half maximum (FWHM) of the CCF, the line Bisector Inverse Slope (BIS), $H\alpha$, and the $\log R'_{\text{HK}}$ converted from the S-index following Suárez Mascareño et al. (2015). RV observations with HARPS-N are still currently ongoing with the GTO programme and will be presented in a mass determination paper at a later date.

2.3 High Resolution Imaging

As part of our standard process for validating transiting exoplanets to assess the possible contamination of bound or unbound companions on the derived planetary radii (Ciardi et al. 2015), we observed

Gliese 12 with high-resolution near-infrared adaptive optics (AO) imaging at Keck Observatory and with optical speckle observations at WIYN.

2.3.1 Optical Speckle at WIYN

We observed Gliese 12 on 2018 November 21 using the NN-EXPLORE Exoplanet Stellar Speckle Imager (NESSI; Scott et al. (2018)) at the WIYN 3.5 m telescope on Kitt Peak. NESSI is a dual-channel instrument and obtains a simultaneous speckle measurement in two filters. In this case, we used filters with central wavelengths of $\lambda_c = 562$ and 832 nm . The speckle data consisted of 5 sets of 1000 40 ms exposures in each filter, centred on Gliese 12. These exposures were limited to a 256×256 pixel readout section in each camera, resulting in a 4.6×4.6 arcsecond field-of-view. Our speckle measurements, however, are further confined to an outer radius of 1.2 arcseconds from the target star due the fact that speckle patterns lose sufficient correlation at wider separation. To calibrate the shape of the PSF, similar speckle data were obtained of a nearby single star immediately prior to the observation of Gliese 12.

We reduced the speckle data using a pipeline described by Howell et al. (2011). Among the pipeline products is a reconstructed image of the field around Gliese 12 in each filter. The reconstructed images are the basis of the contrast curves that set detection limits on additional point sources that may lie in close proximity to Gliese 12. These contrast curves are measured based on fluctuations in the noise-like background level as a function of separation from the target star. The data, including reconstructed images, were inspected to find any detected companion stars to Gliese 12, but none were found. We present the reconstructed images and contrast limits in Figure 2.

2.3.2 Near-Infrared AO at Keck

The observations were made with the NIRC2 instrument on Keck-II behind the natural guide star AO system (Wizinowich et al. 2000) on 2023 August 05 in the standard 3-point dither pattern that is used with NIRC2 to avoid the left lower quadrant of the detector which is typically noisier than the other three quadrants. The dither pattern step size was $3''$ and was repeated twice, with each dither offset from the previous dither by $0.5''$. NIRC2 was used in the narrow-angle mode with a full field of view of $\sim 10''$ and a pixel scale of approximately $0.0099442''$ per pixel. The Keck observations were made in the *Kcont* filter ($\lambda_o = 2.2706$; $\Delta\lambda = 0.0296 \mu\text{m}$) with an integration time in each filter of 1 seconds for a total of 9 seconds. Flat fields were generated from a median average of dark subtracted dome flats. Sky frames were generated from the median average of the 9 dithered

⁵ <https://github.com/njcuk9999/lbl>, version 0.61.0.

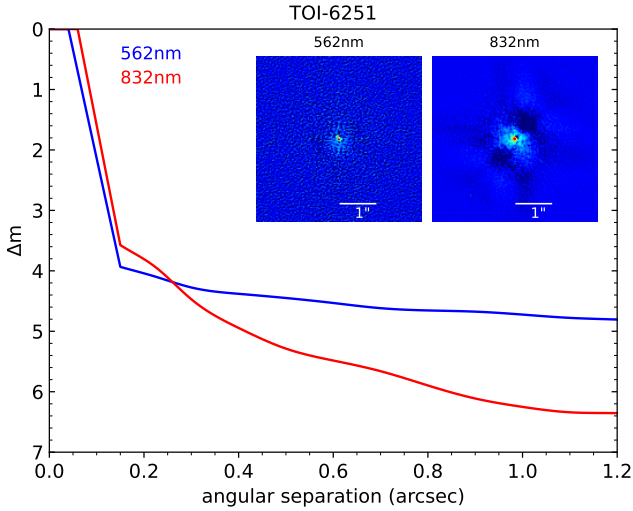


Figure 2. The 5σ contrast curves of WIYN/NESSI speckle high-resolution images at 562 nm (blue) and 832 nm (red), with insets showing the central region of the images centred on Gliese 12.

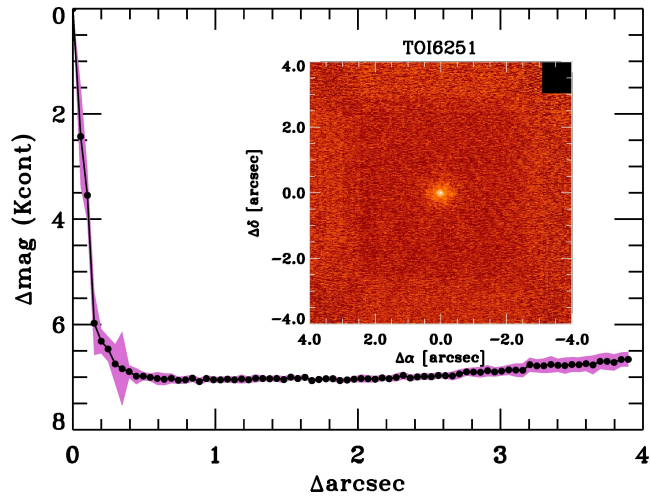


Figure 3. Companion sensitivity for the near-infrared adaptive optics imaging. The black points represent the 5σ limits and are separated in steps of 1 FWHM; the purple represents the azimuthal dispersion (1σ) of the contrast determinations (see text). The inset image is of the primary target showing no additional close-in companions.

science frames; each science image was then sky-subtracted and flat-fielded. The reduced science frames were combined into a single combined image using an intra-pixel interpolation that conserves flux, shifts the individual dithered frames by the appropriate fractional pixels; the final resolution of the combined dithers was determined from the full-width half-maximum of the point spread function; $0.049''$. To within the limits of the AO observations, no stellar companions were detected. The final 5σ limit at each separation was determined from the average of all of the determined limits at that separation and the uncertainty on the limit was set by the rms dispersion of the azimuthal slices at a given radial distance (Figure 3).

Table 4. Stellar parameters of Gliese 12.

Parameter	Value	Reference
Gliese	12	Gliese (1956, 1969)
Giclas (G)	32-5	Giclas et al. (1959, 1971)
LHS	1050	Luyten (1976)
2MASS	00154919+1333218	Skrutskie et al. (2006)
<i>Gaia</i> DR3	2768048564768256512	<i>Gaia</i> DR3
TIC	52005579	Stassun et al. (2019)
TOI	6251	Guerrero et al. (2021)
R.A.	00:15:49.24	<i>Gaia</i> DR3
Declination	+13:33:22.32	<i>Gaia</i> DR3
ϖ (mas)	82.194 ± 0.032	<i>Gaia</i> DR3
Distance (pc)	12.162 ± 0.005	Derived
μ_α (mas yr $^{-1}$)	$+618.065 \pm 0.039$	<i>Gaia</i> DR3
μ_δ (mas yr $^{-1}$)	$+329.446 \pm 0.034$	<i>Gaia</i> DR3
RV (km s $^{-1}$)	$+51.213 \pm 0.0036$	Soubiran et al. (2018)
U (km s $^{-1}$)	-51.11 ± 0.02	This work
V (km s $^{-1}$)	$+27.31 \pm 0.03$	This work
W (km s $^{-1}$)	-31.62 ± 0.04	This work
Spectral Type	M3.5V M4V	Lépine et al. (2013) Newton et al. (2014)
G (mag)	11.399 ± 0.003	<i>Gaia</i> DR3
BP (mag)	12.831 ± 0.003	<i>Gaia</i> DR3
RP (mag)	10.227 ± 0.004	<i>Gaia</i> DR3
B (mag)	14.265 ± 0.038	Stassun et al. (2019)
V (mag)	12.600 ± 0.042	Stassun et al. (2019)
T (mag)	10.177 ± 0.007	Stassun et al. (2019)
J (mag)	8.619 ± 0.002	Skrutskie et al. (2006)
H (mag)	8.068 ± 0.026	Skrutskie et al. (2006)
K_s (mag)	7.807 ± 0.020	Skrutskie et al. (2006)
M (M_\odot)	0.241 ± 0.006	This work
R (R_\odot)	0.269 ± 0.008	This work
ρ (g cm $^{-3}$)	$17.55^{+1.60}_{-1.42}$	This work
$\log g$ (cm s $^{-2}$)	4.96 ± 0.03	This work
T_{eff} (K)	3253 ± 55	This work
L (L_\odot)	0.0074 ± 0.0008	This work
[Fe/H] (dex)	-0.29 ± 0.09	Maldonado et al. (2020)
Age (Gyr)	$7.0^{+2.8}_{-2.2}$	This work
$\log R'_{HK}$	-5.68 ± 0.12	This work

3 STELLAR PROPERTIES

Here we present our determinations of the stellar properties of Gliese 12. Our adopted parameters are summarised in Table 4.

3.1 Stellar parameters

We estimate the mass and radius of Gliese 12 using the empirical relations of Mann et al. (2015, 2019). To begin, we used the K_s -band apparent magnitude from 2MASS (7.807 ± 0.020 mag; Skrutskie et al. 2006) and the stellar distance from the *Gaia* DR3 parallax (12.162 ± 0.005 pc; *Gaia* Collaboration et al. 2023), to derive the corresponding absolute K_s -band magnitude of $M_{K_s} = 7.382 \pm 0.020$ mag. Using Mann et al. (2019, equation 2 and tables 6, 7) we convert this into a stellar mass $M = 0.241 \pm 0.006 M_\odot$ (2.4% uncertainty), and with Mann et al. (2015, table 1 and equation 4) we determine $R = 0.269 \pm 0.008 R_\odot$ (3.0% uncertainty). From these values for the mass and radius we derive the stellar density $\rho = 17.55^{+1.60}_{-1.42}$ g cm $^{-3}$ (9% uncertainty) and surface gravity $\log g = 4.96 \pm 0.03$ cm s $^{-2}$.

Our stellar mass and radius agree well with the values adopted in

the *TESS* Input Catalogue ($M = 0.242 \pm 0.020 M_{\odot}$, $R = 0.269 \pm 0.008 R_{\odot}$; [Stassun et al. 2019](#)), which is unsurprising as the TIC Cool Dwarf list uses the [Mann et al. \(2015, 2019\)](#) M_{K_S} relations to calculate these parameters ([Stassun et al. 2019](#)). However, our estimate for the stellar density has a larger uncertainty than the TIC value ($17.46 \pm 0.12 \text{ g cm}^{-3}$). The constraint on this parameter (0.7% uncertainty) appears implausibly precise considering the mass and radius uncertainties, so we prefer our characterisation of the stellar density precision. As we use priors on the stellar density in our transit fits this bears significance for our global models (on which see Section 5).

To further constrain the fundamental parameters of Gliese 12, we perform a fit to the stellar spectral energy distribution (SED). We use the *astroARIADNE* Python package ([Vines & Jenkins 2022](#)) to fit the broadband photometry of Gliese 12 to the following stellar atmosphere models: BTSettl-AGSS2009 ([Allard et al. 2011](#)), Kurucz ([Kurucz 1992](#)), and Castelli & Kurucz (ATLAS9) ([Castelli & Kurucz 2003](#)). This algorithm uses a Bayesian Model Averaging method to derive best-fit stellar parameters from the weighted average of each model’s output. This is to mitigate the biases present in an individual model that correlate with the star’s spectral type. Additionally, mass and age are estimated via MIST isochrones ([Choi et al. 2016](#)). We assign a broad Gaussian prior of $3376 \pm 157 \text{ K}$ on T_{eff} from the TIC ([Stassun et al. 2019](#)), and a prior of $[\text{Fe}/\text{H}] = -0.29 \pm 0.09$ from [Maldonado et al. \(2020\)](#). From this analysis we find values of $T_{\text{eff}} = 3253 \pm 55 \text{ K}$ and $L = 0.0074 \pm 0.008 L_{\odot}$ for Gliese 12, which we adopt in Table 4.

3.2 Kinematics

We calculate the space velocities of Gliese 12 relative to the Sun following [Johnson & Soderblom \(1987\)](#), adopting stellar positions and velocities as in Table 4. We find $(U, V, W) = (-51.11 \pm 0.02, +27.31 \pm 0.03, -31.62 \pm 0.04) \text{ km s}^{-1}$, where U is defined as positive in the direction of the galactic centre, V is positive towards the galactic rotation, and W is positive in the direction of the north galactic pole. Assuming values for the solar space velocities from [Schönrich et al. \(2010\)](#), we then find space motions relative to the local standard of rest of $(U_{\text{LSR}}, V_{\text{LSR}}, W_{\text{LSR}}) = (-40.0 \pm 0.8, +39.5 \pm 0.5, -24.3 \pm 0.4) \text{ km s}^{-1}$. Following the membership probabilities established by [Bensby et al. \(2003\)](#) these kinematics, in particular the strongly positive value of V_{LSR} , are consistent only with thin disk membership for Gliese 12. However, its kinematics are comparatively hot for a thin disk star; its $V_{\text{tot}} \equiv \sqrt{U_{\text{LSR}}^2 + V_{\text{LSR}}^2 + W_{\text{LSR}}^2} \approx 61 \text{ km s}^{-1}$ belongs to the upper end of values found among nearby M dwarfs ([Newton et al. 2016](#); [Medina et al. 2022](#)). This suggests a relatively old age for Gliese 12.

We may extend this further by employing quantitative *UVW*-age relationships, such as that of [Almeida-Fernandes & Rocha-Pinto \(2018\)](#) or [Veyette & Muirhead \(2018\)](#). These two relations are calibrated to the *UVW* velocity dispersion-versus-isochrone age for Sun-like stars from the Geneva-Copenhagen survey ([Nordström et al. 2004](#); [Casagrande et al. 2011](#)). For the measured *UVW* space velocities of Gliese 12, these relations return kinematic ages of $6.3_{-3.1}^{+4.1} \text{ Gyr}$ ([Almeida-Fernandes & Rocha-Pinto 2018](#)) or $7.0_{-2.2}^{+2.8} \text{ Gyr}$ ([Veyette & Muirhead 2018](#)). These estimates are consistent with an older, most likely super-solar age for Gliese 12. We adopt the age from the [Veyette & Muirhead \(2018\)](#) relation for this star.

3.3 Stellar activity

We measured the S-index of Gliese 12 from the 13 HARPS-N spectra (Table A2) and, following the method outlined in [Suárez Mascareño et al. \(2015\)](#), used them to compute the values of $\log R'_{\text{HK}}$. During the observation span of Gliese 12, we find an average $\log R'_{\text{HK}}$ of -5.68 ± 0.12 . In comparison with the M-dwarf sample studied by [Mignon et al. \(2023\)](#), Gliese 12 lies far towards the lower end of the observed distribution in $\log R'_{\text{HK}}$. The S-index and associated $\log R'_{\text{HK}}$ are traditionally seen as an excellent indicator for a star’s magnetic cycle and overall activity level, implying a low level of stellar activity for Gliese 12.

We also use the average value of $\log R'_{\text{HK}}$ to estimate the expected rotational period of Gliese 12. Using the $\log R'_{\text{HK}} - P_{\text{rot}}$ relation for M3.5-M6 dwarfs from [Suárez Mascareño et al. \(2018\)](#), we find an estimated rotational period of $132_{-25}^{+37} \text{ days}$. We point out that this estimate comes from a calibration relation and that the true rotation period may thus be outside these bounds. The rotational period of Gliese 12 has previously been measured from MEarth photometry as 78.5 d ([Irwin et al. 2011](#)) or 81.2 d ([Newton et al. 2016](#)). There are various possibilities for the discrepancies between the [Suárez Mascareño et al. \(2018\)](#) prediction and measured values, for example, the manifestation of the rotation period in the data may not be the same as the physical rotation period ([Nava et al. 2020](#)). Alternatively, the $\log R'_{\text{HK}}$ of Gliese 12 varies over time due to a magnetic cycle ([Mignon et al. 2023](#)), therefore if it has been presently observed at a low value, then the predicted rotational period could be brought into agreement with the observed one.

Finally, we performed a Bayesian generalised Lomb-Scargle (BGLS) analysis ([Boisse et al. 2011](#); [Mortier et al. 2015](#)) on the *TESS* SAP and PDCSAP photometry to search for any stellar variability, but did not detect any significant modulation. However, this analysis is adversely affected by the short $\sim 27\text{d}$ baseline of the *TESS* sectors. Visual inspection of the *TESS* lightcurves also shows no significant evidence for flares, which is expected for inactive M dwarfs in *TESS* ([Medina et al. 2020](#)) and consistent with a low magnetic activity level for Gliese 12. This is consistent with the picture of an old stellar age ([Medina et al. 2022](#)).

4 PLANET VALIDATION

To ascertain the planetary nature of Gliese 12 b, we enumerate below several false positive scenarios that we can rule out from the available evidence:

(i) **The discovery transit event is not an artifact of *TESS* instrument systematics:** We can rule this out from five independent *CHEOPS* visits and three ground-based observations that successfully detect a transit.

(ii) **Gliese 12 b is not a stellar companion:** The radial velocities from the TRES spectra, presented in Table A1, vary by only 50 ms^{-1} , largely ruling out a stellar companion and motivating further observations with HARPS-N. From our HARPS-N radial velocity measurements outlined in Section 2.2.2 and presented in Table A2, we find that the data has an RMS of only 2.60 m/s. From the peak-to-peak scatter in the RV observations, we can place an upper limit on the companion mass of $< 10 M_{\oplus}$, well below the substellar limit. We also use TRICERATOPS ([Giacalone et al. 2021](#)) to estimate the False Positive Probability (FPP) for Gliese 12 b. From TRICERATOPS we obtain a very low false positive probability

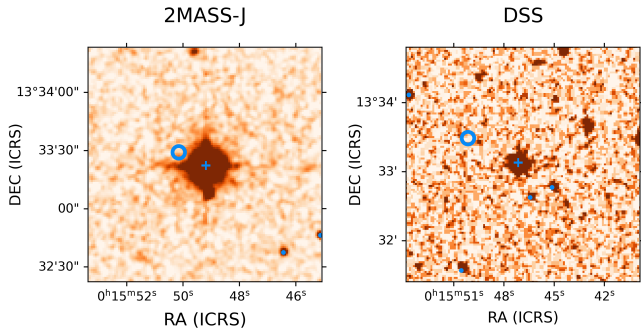


Figure 4. Historical images of the field surrounding Gliese 12. **Left:** 2MASS J band image from 1998 (Skrutskie et al. 2006) **Right:** DSS image from 1949 (Lasker et al. 1990). The blue circle indicate the location of Gliese 12 when it was observed by *TESS*. The blue cross indicates the location of Gliese 12 when it was observed by 2MASS. Blue dots indicate all the other stars in the field of view within ΔT Mag 7.5 of Gliese 12. A background eclipsing binary that can mimic the 1.1 ppt transit signal needs to be within ΔT Mag 7.5 of Gliese 12. These images can be used to rule out the existence of such stars when *TESS* is observing Gliese 12.

of $< 5 \times 10^{-4}$.

(iii) **The transit event is not caused by a background eclipsing binary:** We can preclude this scenario from archival imaging and high proper motion of Gliese 12. In archival images of Gliese 12 taken by DSS and 2MASS, we see no resolved sources in the *TESS* epoch sky position of Gliese 12 within $\Delta T < 7.6$ mag out to 25 arcseconds (Figure 4). This is the minimum brightness difference required of an eclipsing binary to generate an eclipse that can be diluted to our observed transit depth of 1.1 ppt. We note that no sources exist in the Gaia Archive (Gaia Collaboration et al. 2023) within 25 arcseconds down to G mag 20. Any resolvable sources within this radius would be too faint to cause significant contamination in the transit photometry. In addition, our high resolution AO (Section 2.3) reveals no companion sources within ΔK mag of 6.5 farther than 0.5 arcsec from Gliese 12. The SPOC data validation difference image centroid offset (Twicken et al. 2018) locates the source of the transit signal within 9.9 ± 8.5 arcsec of Gliese 12 and excludes all TIC objects within ΔT mag of 7.6 as potential transit sources.

(iv) **Gliese 12 b does not host a widely separated companion that is an eclipsing binary:** If the flux from Gliese 12 were diluted by a bound hierarchical companion, the spectra in Section 2.2.2 would reveal its presence unless it were smaller than Gliese 12. Our False Positive Probability estimate with TRICERATOPS incorporates a computation of the probability of this scenario (PEB and PEBx2P) from the shape of the transit model. Our low FPP from TRICERATOPS therefore constrains this scenario as well. Furthermore, our high resolution adaptive optics and speckle imaging in Section 2.3 reveal no companion sources down to K mag = 13.8 at 0.2 arcseconds. We can therefore confidently rule this scenario out.

5 PLANET MODELLING

We model the transits of Gliese 12 b using the available photometry from *TESS*, *CHEOPS*, MINERVA, and SPECULOOS. We first obtain our prior on the stellar density ρ from Table 4 to apply to our transit model.

Using the ensemble MCMC implemented in emcee (Foreman-Mackey et al. 2013), we simultaneously model the transit and apply least-squares detrending for the *CHEOPS*, MINERVA, and SPECULOOS data. We use the transit model from Mandel & Agol (2002), implemented by Kreidberg (2015) in the BATMAN package, supersampling by a factor of 2 for the *TESS* 20s cadence data, by a factor of 12 for the *TESS* 120s cadence data, and by a factor of 4 for all *CHEOPS* and ground-based data. We sample different quadratic limb darkening coefficients for the different bandpasses of the *TESS*, *CHEOPS*, MINERVA, SPECULOOS, and PMO photometry respectively. We obtain gaussian prior means and standard deviations on limb darkening coefficients from Claret (2017, 2021), using values from Table 4 for T_{eff} , $\log g$, and metallicity. For the *TESS*, *CHEOPS*, MINERVA, SPECULOOS, and PMO data we adopt *TESS*, *CHEOPS*, full optical, and Sloan r' filter bandpasses respectively in order to generate our prior.

We additionally used dynamic nested sampling through the PyORBIT⁶ package (Malavolta et al. 2016, 2018), which uses dynesty (Speagle 2020) to model planetary and stellar activity signals and obtain best-fit activity and planet parameters. PyORBIT makes use of the BATMAN python package for fitting the transit to the photometric data, where we assumed a quadratic stellar intensity profile for fitting the limb darkening coefficients, and an exposure time of 20.0 s for the *TESS* observations in sectors 42, 43, and 57, 120.0 s for *TESS* sector 70, 30.0 s for the *CHEOPS* observations, 30.0 s and 60.0 s for the MINERVA telescopes 1 and 2 observations respectively, 10.0 s for the Europa, Ganymede, and Io SPECULOOS observations, and 55.0 s for the PMO observations, as inputs to the light curve model. The priors placed on the limb-darkening coefficients were calculated using interpolation from Claret (2017, table 25) for the *TESS* light curves and from Claret (2021, table 8) for the *CHEOPS* light curves. For the emcee fit we apply Gaussian priors on limb darkening, while for the dynesty fit we apply these as Uniform priors. This is because recent empirical constraints have been in conflict with standard theoretical estimates of limb darkening for cool stars (Patel & Espinoza 2022). We therefore use the PyORBIT model as confirmation that these potential problems do not significantly impact our posterior estimates.

Inferred planetary parameters from the fit for both emcee and dynesty are shown in Table 5, alongside the priors implemented. We find that the results of the two methods are consistent to 1σ across all planetary parameters. We note that a difference in errors for our derived planetary radii is due to differences in our sampling techniques' tendencies to handle deviations from Gaussianity in our posterior distributions. We adopt our final parameters from the model with the more conservative parameter uncertainty on R_p , which is the emcee fit. From this we find Gliese 12 b to be a small, temperate ($1.0 \pm 0.1 R_{\oplus}$, 315 ± 5 K) planet with a 12.76144 ± 0.00006 d orbital period. Figure 5 shows the phase-folded light curves for the *TESS*, *CHEOPS*, MINERVA, SPECULOOS, and PMO data along with the best-fitting transit models using emcee sampling method. The phase-folded light curves and best-fitting transit models obtained from the dynesty sampling method for the data can be found in Appendix B in Figure B1.

⁶ <https://github.com/LucaMalavolta/PyORBIT>, version 8.

Table 5. Planetary properties calculated from the combined transit fit. All limb darkening priors are normal for emcee and uniform for dynesty. We adopt the emcee values due to the more conservative parameter uncertainty on R_p .

Parameter	emcee	dynesty	Source
Fitted Parameters			
T_0 (BJD)	2459497.184 ± 0.003	2459497.182 ^{+0.003} _{-0.002}	Measured (Uniform prior)
P (days)	12.76144 ± 0.00006	12.76142 ^{+0.00005} _{-0.00006}	Measured (Uniform prior)
R_p/R_*	0.034 ± 0.002	0.031 ± 0.001	Measured (Uniform prior)
b	0.80 ± 0.07	0.67 ^{+0.04} _{-0.05}	Measured (Uniform prior)
ρ_* (g/cm ³)	17.4 ± 0.6	17.4 ^{+1.3} _{-1.4}	Measured (Normal prior from Table 4)
a/R_*	53.1 ± 0.6	53.4 ^{+1.5} _{-1.6}	Measured (Uniform prior)
Derived Properties			
R_p (R_\oplus)	1.03 ± 0.11	0.91 ± 0.04	Derived
i (degrees)	89.12 ± 0.07	89.28 ^{+0.06} _{-0.05}	Derived
a (AU)	0.066 ± 0.002	0.067 ± 0.003	Derived
T_{eq} (K)	315 ± 5	315 ± 10	Derived (assuming $A_B=0$)
T_{eq} (K)	287 ± 5	290 ± 9	Derived (assuming $A_B=A_\oplus$)
F (S_\oplus)	1.6 ± 0.2	1.6 ± 0.2	Derived
Limb Darkening Coefficients			
q1 _{TESS}	0.40 ± 0.20	0.60 ^{+0.27} _{-0.32}	Measured (Claret (2017) prior)
q2 _{TESS}	0.12 ± 0.07	0.32 ^{+0.35} _{-0.23}	Measured (Claret (2017) prior)
q1 _{CHEOPS}	0.60 ± 0.10	0.35 ^{+0.27} _{-0.22}	Measured (Claret (2021) prior)
q2 _{CHEOPS}	0.17 ± 0.06	0.64 ^{+0.26} _{-0.38}	Measured (Claret (2021) prior)
q1 _{MINERVA}	0.60 ± 0.10	0.60 ^{+0.27} _{-0.35}	Measured
q2 _{MINERVA}	0.21 ± 0.06	0.53 ^{+0.32} _{-0.35}	Measured
q1 _{SPECULOOS}	0.70 ± 0.20	0.71 ^{+0.21} _{-0.33}	Measured
q2 _{SPECULOOS}	0.26 ± 0.07	0.61 ^{+0.28} _{-0.37}	Measured
q1 _{PMO}	0.50 ± 0.20	0.53 ^{+0.32} _{-0.36}	Measured
q2 _{PMO}	0.26 ± 0.07	0.51 ^{+0.33} _{-0.34}	Measured

6 DISCUSSION

6.1 Prospects for mass measurement and interior composition

We use the results of the global photometric analysis (see Table 5) to predict the expected planetary mass and radial velocity semi-amplitude of the planet. Otegi et al. (2020) present a mass-radius relation that is dependent on the density of the planet (ρ_b):

$$M_b [M_\oplus] = (0.90 \pm 0.06) R_b^{(3.45 \pm 0.12)} \text{ if } \rho_b > 3.3 \text{ g cm}^{-3} \quad (1)$$

The high density case is applicable when the planet has a rocky composition, and assuming this, the planet would have a mass of $0.88^{+0.39}_{-0.26} M_\oplus$, leading to a semi-amplitude of only $0.57^{+0.26}_{-0.17} \text{ ms}^{-1}$.

Given the brightness of the star, $V(\text{mag}) = 12.600 \pm 0.042$, and following the early observations from HARPS-N, the predicted precision on the RV measurements with continued HARPS-N observations is 1.15 ms^{-1} with a 30min integration time. The planetary signal should thus be detectable with sufficient observations taken with a high-resolution high-stability spectrograph. Assuming a circular orbit and no correlated noise, we calculate that for a 3σ mass detection approximately 200 HARPS-N RV observations would be needed, with 30mins per observation, leading to a total of approximately 100 hours of telescope time. For a 5σ mass detection, approximately 600 RV observations would be needed, leading to 300hrs of telescope time. Whilst these calculations are specific to HARPS-N, there are

other instruments capable of doing this, including those with better stability such as ESPRESSO.

The above estimates might be slightly optimistic since they ignore the possible impact of stellar activity. However, we highlight that thanks to the low activity level of Gliese 12, the expected stellar-induced RV RMS should only be $0.27^{+0.25}_{-0.14} \text{ ms}^{-1}$ (using an extrapolation of the relations in Hojjatpanah et al. (2020)). This allows for the small planetary signal to be detectable in the data. Additional planets in the system, including non-transiting ones, may also be detectable through RV observations as multi-planet systems are common for M dwarfs, and compact multi-systems are also more common around low-metal stars (Anderson et al. 2021), such as Gliese 12.

With a measured mass and thus bulk density, the planet's interior structure can be studied. The density and internal structures of Earth-like planets around metal-poor stars, such as Gliese 12 b, is important as recent observational studies have found potential compositional trends (Wilson et al. 2022; Chen et al. 2022) that may be imprints of planet formation or evolution (Owen & Jackson 2012; Owen & Murray-Clay 2018). Adibekyan et al. (2021) found that planet density is correlated with stellar iron mass fraction for Earth-like bodies, which provides evidence that the stellar compositional environment affects planetary internal structure. Different interior structure compositions due to formation environment variations could impact potential habitability (Foley & Driscoll 2016). Planets around metal-poor stars may have small metallic cores and

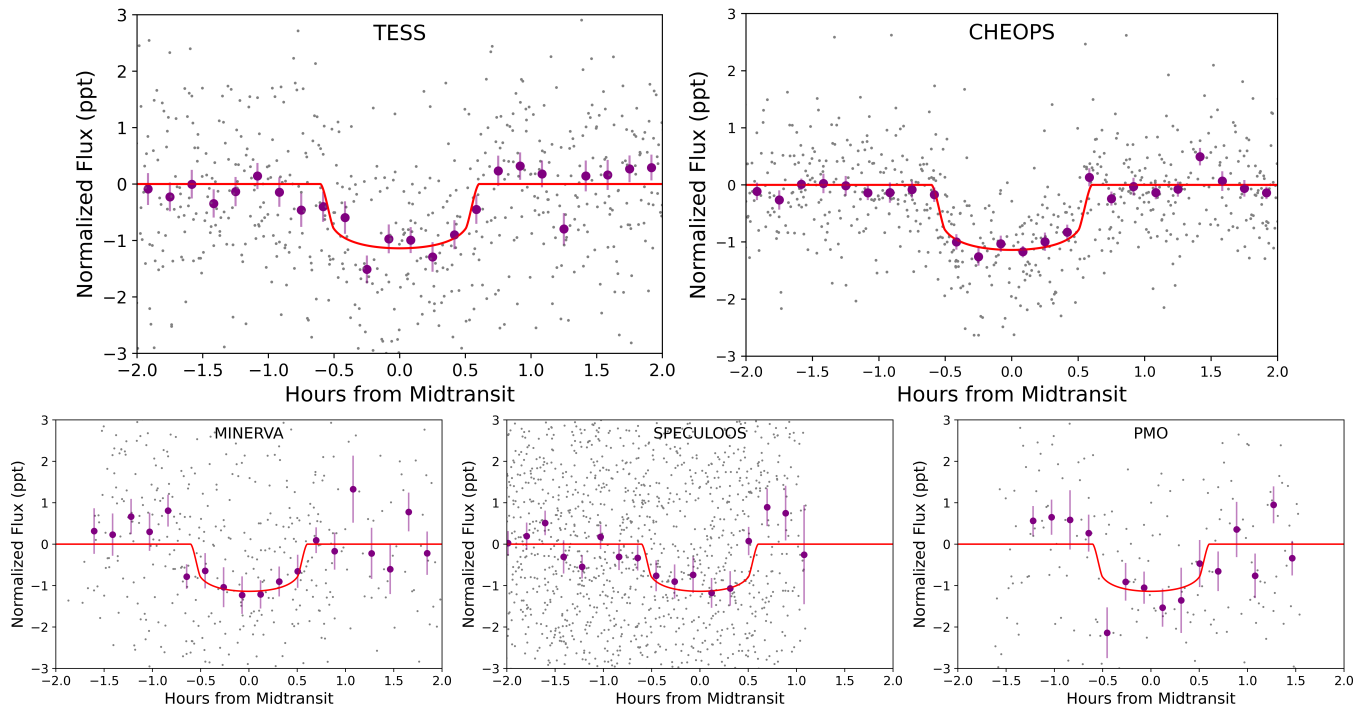


Figure 5. Phased transits of Gliese 12 b from fit results obtained with *emcee*. The red lines represent the transit from the best fit MCMC model. The purple data points are binned into 10 minute intervals for TESS and CHEOPS and 11.5 minute intervals for the ground-based data. The top left panel shows five phased TESS transits, with the grey points representing the data binned down to 2 minute cadence. The top right panel shows five phased CHEOPS transits of this target. The bottom left panel shows the MINERVA-Australis data. The bottom-center panel shows the SPECULOOS data, and the bottom right panel shows the PMO data.

larger mantles compared to Earth and thus have weaker magnetic fields and increased volcanism. However, this is not well-understood as in the low-metallicity regime this trend is only anchored by two well-characterised planets (Mortier et al. 2020; Lacedelli et al. 2022), with none as small or cold as Earth. Therefore, by combining our precise radius measurement with an accurately measured mass of Gliese 12 b, we will be able to potentially verify a fundamental underlying process sculpting small planets, including our own Earth, across the Galaxy.

6.2 Prospects for atmospheric characterisation

Gliese 12 b is among the most amenable temperate ($1.6 \pm 0.2 S_{\oplus}$), terrestrial ($1.0 \pm 0.1 R_{\oplus}$) planets for atmospheric spectroscopy discovered to date. Its proximity to the Solar System (12 pc), high apparent brightness ($K = 7.8$ mag), and relatively low activity level make it an ideal candidate for future transmission spectroscopy with *JWST*. It is also unique in its parameter space for being exceptionally bright yet temperate (Figure 6), making it ideal for characterisation.

So far, the TRAPPIST-1 system (Gillon et al. 2017) and the TOI-700 system (Gilbert et al. 2020; Rodriguez et al. 2020; Gilbert et al. 2023) have been the most well-studied exoplanet systems harbouring Earth-sized, temperate planets ($\lesssim 500\text{K}$, $\lesssim 1.6R_{\oplus}$). The *JWST* emission spectrum of TRAPPIST-1c disfavors a thick CO_2 dominated atmosphere, although the presence of higher molecular weight species cannot be constrained (Zieba et al. 2023). Other temperate planets in the TRAPPIST-1 system are planned to be targeted in *JWST* transmission and emission spectroscopy. The Transmission Spectroscopy Metric (TSM; Kempton et al. (2018)) was created as a heuristic to assess the amenability of TESS planets to transmission

spectroscopy measurements. The TSM value of Gliese 12 b, using the mass-radius relation presented in Equation 1 is approximately 20. In comparison, the TRAPPIST-1 planets d, e, f, g and h present TSM values between 15 and 25. The TOI-700 system, however, has been shown to be just out of the reach of *JWST*'s capabilities (Suissa et al. 2020), with a TSM of less than 5. Gliese 12 is both closer, brighter, and lower activity than TRAPPIST-1 or TOI-700, enabling uniquely constraining observations of its planet's atmosphere.

Just outside these equilibrium temperature and/or planetary radius bounds, *JWST* transmission spectroscopy has returned mixed results for atmospheric detection on different planets around M dwarfs. LHS 475 b, though much hotter than Gliese 12 b, has been observed to have a featureless spectrum by *JWST* so far (Lustig-Yaeger et al. 2023). For the hot super-Earth GJ 486b, the *JWST* transmission spectrum contains tantalising features that may be interpreted either as a water rich atmosphere or contamination from unocculted starspots (Moran et al. 2023).

Contamination from stellar activity represents an important noise floor for detections of atmospheres around terrestrial planets, particularly for terrestrial planets around M dwarfs (Rackham et al. 2018). Most M dwarfs and many other stars present non-uniform stellar photospheres due to the presence of large spots. These spots typically introduce photometric variability on a scale greater than 1% of the total stellar flux. For these stars, unocculted spots introduce positive features in transmission spectra, which can mimic signatures due to molecular absorption in the planet's atmosphere (e.g. Moran et al. 2023). This problem has been noted recently with *JWST* in efforts to constrain temperate, terrestrial planet atmospheres for the TRAPPIST-1 system (Lim et al. 2023). Gliese 12 is well monitored by both ground based photometry and spectroscopy, showing a low activity level for M dwarfs and slow rotation in comparison to the

Mignon et al. (2023) sample which featured only 7 stars with a lower $\log R'_{HK}$ (Section 3.3). Compared to the other similar systems, such as TOI-700 and TRAPPIST-1, the lack of visible starspot variability in the light curves, very low magnetic activity indicators, and slow rotation means that contamination in the planetary spectra from stellar spots will likely be far lower, making any interpretation of spectra features more tractable.

Whilst no high molecular weight atmosphere has yet been detected on such a planet, the atmospheres of Venus and the Earth in the Solar System hint at the possible diversity of such atmospheres elsewhere. M dwarfs are the most numerous stellar type in our galaxy, and terrestrial planets around them are commonplace (Dressing & Charbonneau 2015). The atmospheric compositions of true solar system analogues will be inaccessible for the foreseeable future. Therefore, studies of cool, rocky planets around M dwarfs – similar in insolation and mass to Earth and Venus – will provide insight into the formation of our Solar System and the diverse atmospheres of the terrestrial planets. H_2O , CO_2 , and CH_4 features in the atmospheres of such planets would also be accessible to JWST (Wunderlich et al. 2019).

A key question in the study of the habitability of planets around M dwarfs is these planets' capacity to retain an atmosphere in the face of high stellar activity. Due to high XUV flux and flares from the stars, it has been hypothesised that the planetary atmospheres are photoevaporated efficiently, even for temperate planets (e.g. Lincowski et al. 2018; Zahnle & Catling 2017). The degree and extent to which this occurs is still poorly understood. JWST atmospheric studies of Gliese 12 b therefore presents a valuable opportunity to make constraining measurements of a temperate, terrestrial planet's atmosphere, towards understanding the requisites of habitability for planets around M dwarfs.

6.3 Prospects for Habitability

As the closest temperate, Earth-sized transiting planet to the Solar System, a key open question is the potential for Gliese 12 b to maintain temperatures suitable for liquid water to exist on its surface. With an insolation between the Earth and Venus's ($F = 1.6 \pm 0.2 S_{\oplus}$), this planet's surface temperature would be highly dependant on its atmospheric conditions. It is also unknown whether Gliese 12 b is tide-locked or exists in a spin-orbit resonance, which may also impact the retention of water in the planet's evolutionary history (Pierrehumbert & Hammond 2019). Gliese 12 b occurs just inward of the habitable zone as defined by Kopparapu et al. (2013) due to the predicted efficiency of water-loss around M dwarfs. However, Gliese 12 b may well be within the Recent Venus limit of its host star (Figure 7) with an insolation flux of $F = 1.6 \pm 0.2 S_{\oplus}$, less than 1σ away from the $1.5 S_{\oplus}$ limit calculated from Kopparapu et al. (2013). This limit is regarded in that analysis as an optimistic habitable zone due to Venus's potential for habitability in the past history of the Solar system. Thus the available evidence does not rule out that Gliese 12 b is potentially habitable.

Due to its proximity to the Recent Venus limit, this target may be a valuable calibration point for theoretical estimates of water-loss, which define the inner edge of the habitable zone. In particular, Gliese 12 b is well suited to study the divergent evolutionary pathways of the atmospheres of Earth and Venus. While Earth retained its water, the runaway greenhouse effect on Venus led to water escape and photo-dissociation (Ingersoll 1969). If a runaway greenhouse effect is in progress, signatures may be detectable in the UV band as an extended hydrogen exosphere (Bourrier et al. 2017a,b). A null detection of water could hint that such a process has already occurred, as on Venus. On the other hand, a detection of water would imply

that the water-loss boundary is inward of the estimates by Kopparapu et al. (2013).

7 CONCLUSIONS

In this paper, we have reported on the discovery and validation of a temperate Earth-sized planet transiting the nearby M dwarf Gliese 12. During *TESS* sectors 43, 57, only 3 transits of the planet were observed, with no transits observed in sector 42. This allowed for a period of 12.76 d or 25.5 d, but with the further addition of *TESS* sector 70 and *CHEOPS* follow-up we were able to determine the actual period. Combining these transits with further ground-based photometry from MINERVA, SPECULOOS, and PMO allowed us to determine precise planetary parameters for Gliese 12 b, indicating that Gliese 12 b is a $1.0 \pm 0.1 R_{\oplus}$ planet with a 12.76144 ± 0.00006 day period, and an effective temperature lower than that of the majority of known exoplanets ($\sim 315K$).

Gliese 12 b is therefore a prime target for future detailed characterisation studies. Its prospects for a precise mass measurement are reasonable and the star has some of the lowest activity levels amongst known M dwarfs. It is also a unique candidate for both atmospheric and stellar study. Further analysis of the Gliese 12 system will allow us to understand evolutionary and compositional trends, which is important as we try to infer the number of true-Earth analogues on our journey to understanding our own place in the Universe.

ACKNOWLEDGEMENTS

CXH and AV are supported by ARC DECRA project DE200101840. VVE is supported by UK's Science & Technology Facilities Council (STFC) through the STFC grants ST/W001136/1 and ST/S000216/1.

This paper includes data collected by the *TESS* mission, which are publicly available from the Mikulski Archive for Space Telescopes (MAST). Funding for the *TESS* mission is provided by NASA's Science Mission directorate. We acknowledge the use of public *TESS* Alert data from pipelines at the *TESS* Science Office and at the *TESS* Science Processing Operations Center. Resources supporting this work were provided by the NASA High-End Computing (HEC) Program through the NASA Advanced Supercomputing (NAS) Division at Ames Research Center for the production of the SPOC data products.

This work makes use of data from the European Space Agency (ESA) *CHEOPS* mission, acquired through the *CHEOPS* AO-4 Guest Observers Programmes ID:07 (PI: Palethorpe) and ID:12 (PI: Verner). *CHEOPS* is an ESA mission in partnership with Switzerland with important contributions to the payload and the ground segment from Austria, Belgium, France, Germany, Hungary, Italy, Portugal, Spain, Sweden and the United Kingdom. We thank support from the *CHEOPS* GO Programme and Science Operations Centre for help in the preparation and analysis of the *CHEOPS* observations. This research has made use of the Exoplanet Follow-up Observation Program (ExoFOP) website, which is operated by the California Institute of Technology, under contract with the National Aeronautics and Space Administration under the Exoplanet Exploration Program.

This work makes use of data from MINERVA-Australis. MINERVA-Australis is supported by Australian Research Council LIEF Grant LE160100001, Discovery Grants DP180100972 and DP220100365, Mount Cuba Astronomical Foundation, and institutional partners University of Southern Queensland, UNSW Sydney, MIT, Nanjing University, George Mason University, University of

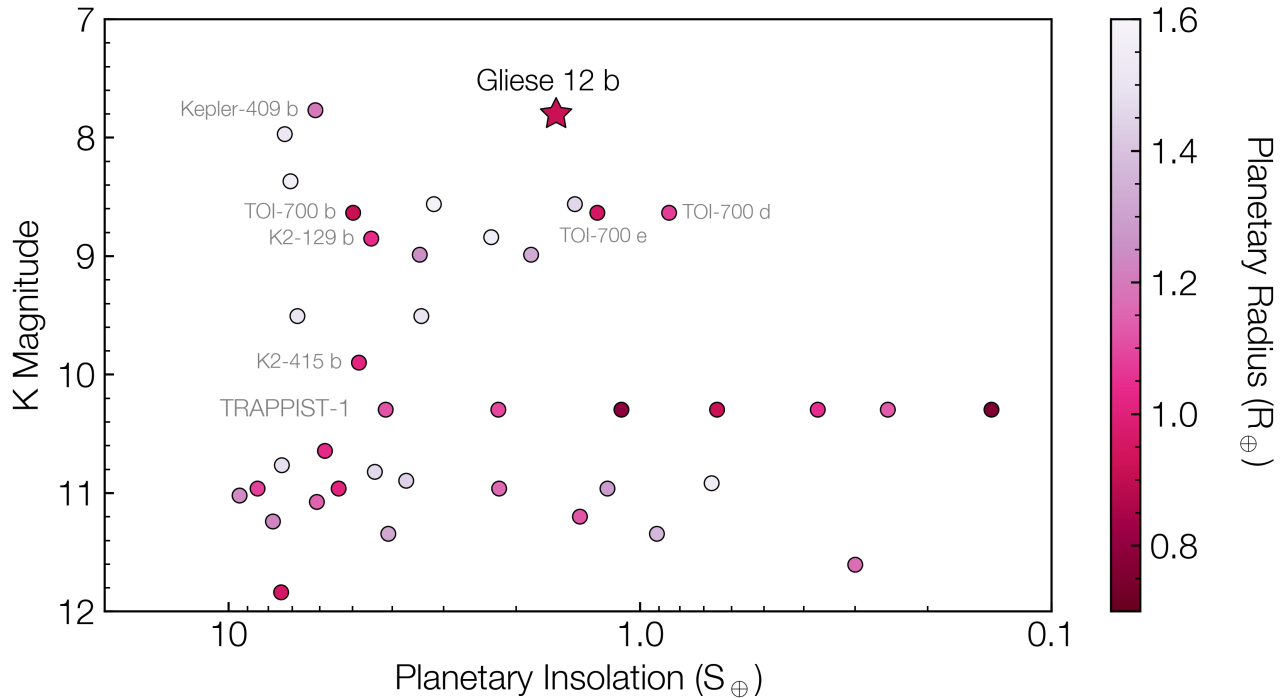


Figure 6. Gliese 12 is amongst the brightest stars (in K band) hosting a temperate Earth-sized planet. Only planets with radii between $0.7 - 1.6 R_{\oplus}$ and insolation flux between 0.1 and $10 S_{\oplus}$ on the Exoplanet Archive as of 03/01/2024 are shown in the figure. The star represents Gliese 12 b and other notable Earth-sized planets are labeled. The TRAPPIST-1 planets in order from left to right are b, c, d, e, f, g, and h.

Louisville, University of California Riverside, University of Florida, and The University of Texas at Austin. We acknowledge and pay respect to Australia’s Aboriginal and Torres Strait Islander peoples, who are the traditional custodians of the lands, waterways and skies all across Australia. In particular, we pay our deepest respects to all Elders, ancestors and descendants of the Giabal, Jarowair, and Yuggera nations, upon whose lands the MINERVA-Australis facility is situated.

We thank Ye Yuan and Jian Chen for their assistance in obtaining and reducing the Purple Mountain Observatory photometry data.

Based on data collected by the SPECULOOS-South Observatory at the ESO Paranal Observatory in Chile. The ULiege’s contribution to SPECULOOS has received funding from the European Research Council under the European Union’s Seventh Framework Programme (FP/2007-2013) (grant Agreement n° 336480/SPECULOOS), from the Balzan Prize and Francqui Foundations, from the Belgian Scientific Research Foundation (F.R.S.-FNRS; grant n° T.0109.20), from the University of Liege, and from the ARC grant for Concerted Research Actions financed by the Wallonia-Brussels Federation. This work is supported by a grant from the Simons Foundation (PI Queloz, grant number 327127). This research is in part funded by the European Union’s Horizon 2020 research and innovation programme (grants agreements n° 803193/BEBOP), and from the Science and Technology Facilities Council (STFC; grant n° ST/S00193X/1, and ST/W000385/1). The material is based upon work supported by NASA under award number 80GSFC21M0002. This publication benefits from the support of the French Community of Belgium in the context of the FRIA Doctoral Grant awarded to M.T. This publication benefits from the support of the French Community of Belgium in the context of the FRIA Doctoral Grant awarded to M.T.

Some of the data presented herein were obtained at Keck Observatory, which is a private 501(c)3 non-profit organization operated as a scientific partnership among the California Institute of Technology, the University of California, and the National Aeronautics and Space Administration. The Observatory was made possible by the generous financial support of the W. M. Keck Foundation. The authors wish to recognize and acknowledge the very significant cultural role and reverence that the summit of Maunakea has always had within the Native Hawaiian community. We are most fortunate to have the opportunity to conduct observations from this mountain.

The HARPS-N project was funded by the Prodex Program of the Swiss Space Office (SSO), the Harvard University Origin of Life Initiative (HUOLI), the Scottish Universities Physics Alliance (SUPA), the University of Geneva, the Smithsonian Astrophysical Observatory (SAO), the Italian National Astrophysical Institute (INAF), University of St. Andrews, Queen’s University Belfast, and University of Edinburgh.

This work has made use of data from the European Space Agency (ESA) mission *Gaia* (<https://www.cosmos.esa.int/gaia>), processed by the *Gaia* Data Processing and Analysis Consortium (DPAC, <https://www.cosmos.esa.int/web/gaia/dpac/consortium>). Funding for the DPAC has been provided by national institutions, in particular the institutions participating in the *Gaia* Multilateral Agreement. This research has made use of the SIMBAD database and VizieR catalogue access tool, operated at CDS, Strasbourg, France. This research has made use of NASA’s Astrophysics Data System. This research has made use of the NASA Exoplanet Archive, which is operated by the California Institute of Technology, under contract with the National Aeronautics and Space Administration under the Exoplanet Exploration Program.

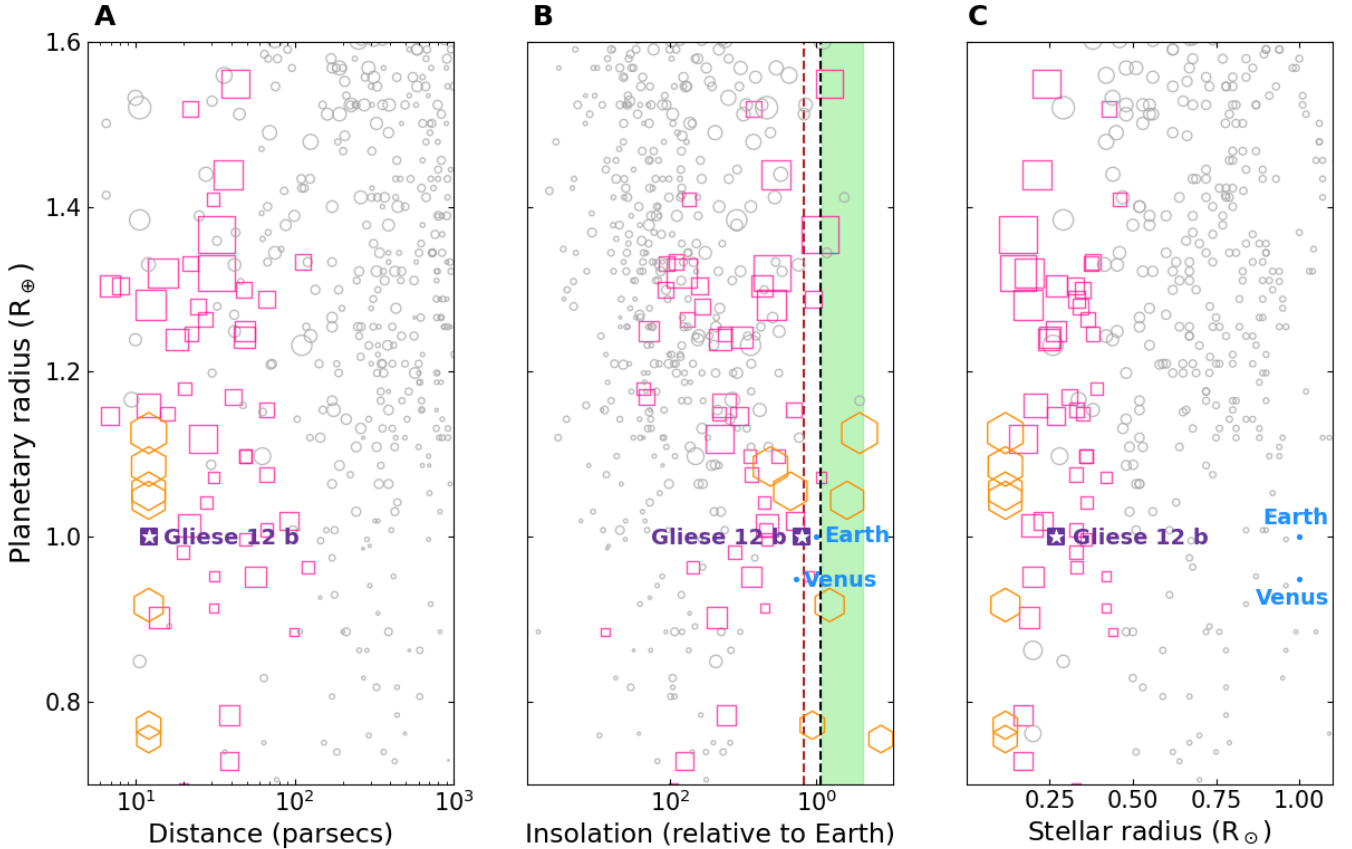


Figure 7. Planetary radius versus distance, insolation, and stellar radius, respectively. Planets were taken from the Extrasolar Planets Encyclopaedia, with those orbiting M dwarfs highlighted as pink squares, and the rest shown as grey circles. Gliese 12 b is highlighted by the white star in the purple square. The orange hexagons correspond to the TRAPPIST-1 planets; nearby planets around small stars that are most accessible to characterization by the James Webb Space Telescope (*JWST*). The green shaded region in **B** is the M-dwarf habitable zone, the black dashed line corresponds to a runaway greenhouse atmosphere, and the dark red dashed line corresponds to recent Venus (Kopparapu et al. 2013). We note that this habitable zone is only appropriate for planets orbiting M dwarfs. The size of each marker is proportional to the transit depth and hence observational accessibility.

This research has made use of the Exoplanet Follow-up Observation Program (ExoFOP; DOI: 10.26134/ExoFOP5) website, which is operated by the California Institute of Technology, under contract with the National Aeronautics and Space Administration under the Exoplanet Exploration Program.

This research is based on photographic data obtained using Oschin Schmidt Telescope on Palomar Mountain. The Palomar Observatory Sky Survey was funded by the National Geographic Society. The Oschin Schmidt Telescope is operated by the California Institute of Technology and Palomar Observatory. The plates were processed into the present compressed digital format with their permission. The Digitized Sky Survey was produced at the Space Telescope Science Institute (ST ScI) under US Government grant NAG W-2166.

L.D. thanks the Belgian Federal Science Policy Office (BELSPO) for the provision of financial support in the framework of the PRODEX Programme of the European Space Agency (ESA) under contract number 4000142531.

KR is grateful for support from UK’s Science and Technology Facilities Council (STFC) via consolidated grant ST/V000594/1.

DAT acknowledges the support of the Science and Technology Facilities Council (STFC).

The ULiege’s contribution to SPECULOOS has received funding from the European Research Council under the European Union’s Seventh Framework Programme (FP/2007-2013) (grant

Agreement n° 336480/SPECULOOS), from the Balzan Prize and Francqui Foundations, from the Belgian Scientific Research Foundation (F.R.S.-FNRS; grant n° T.0109.20), from the University of Liege, and from the ARC grant for Concerted Research Actions financed by the Wallonia-Brussels Federation. MG is F.R.S.-FNRS Research Director.

This research has made use of data obtained from or tools provided by the portal exoplanet.eu of The Extrasolar Planets Encyclopaedia.

DATA AVAILABILITY

This paper includes raw data collected by the *TESS* mission, which are publicly available from the Mikulski Archive for Space Telescopes (MAST, <https://archive.stsci.edu/tess>). Raw data collected by *CHEOPS* can be found using the file keys in Table 1 at https://cheops-archive.astro.unige.ch/archive_browser/. Observations made with HARPS-N on the Telescopio Nazionale Galileo 3.6m telescope are available in Table A2 in the Appendix Section A. Observations made with TRES are available in Table A1 also in Appendix Section A.

REFERENCES

- Addison B., et al., 2019, *PASP*, **131**, 115003
- Adibekyan V., et al., 2021, *A&A*, **649**, A111
- Allard F., Homeier D., Freytag B., 2011, in Johns-Krull C., Browning M. K., West A. A., eds, *Astronomical Society of the Pacific Conference Series* Vol. 448, 16th Cambridge Workshop on Cool Stars, Stellar Systems, and the Sun. p. 91
- Almeida-Fernandes F., Rocha-Pinto H. J., 2018, *MNRAS*, **476**, 184
- Anderson S. G., Dittmann J. A., Ballard S., Bedell M., 2021, *AJ*, **161**, 203
- Artigau É., et al., 2022, *AJ*, **164**, 84
- Bensby T., Feltzing S., Lundström I., 2003, *A&A*, **410**, 527
- Benz W., et al., 2021, *Experimental Astronomy*, **51**, 109
- Bertaux J. L., Lallement R., Ferron S., Boonne C., Bodichon R., 2014, *A&A*, **564**, A46
- Boisse I., Bouchy F., Hébrard G., Bonfils X., Santos N., Vauclair S., 2011, *A&A*, **528**, A4
- Bourrier V., et al., 2017a, *A&A*, **599**, L3
- Bourrier V., et al., 2017b, *A&A*, **602**, A106
- Brady M. T., Bean J. L., 2022, *AJ*, **163**, 255
- Buchhave L. A., et al., 2010, *ApJ*, **720**, 1118
- Burt J. A., et al., 2021, *AJ*, **162**, 87
- Casagrande L., Schönrich R., Asplund M., Cassisi S., Ramírez I., Meléndez J., Bensby T., Feltzing S., 2011, *A&A*, **530**, A138
- Castelli F., Kurucz R. L., 2003, in Piskunov N., Weiss W. W., Gray D. F., eds, Vol. 210, *Modelling of Stellar Atmospheres*. p. A20 ([arXiv:astro-ph/0405087](https://arxiv.org/abs/astro-ph/0405087))
- Chen L.-H., Pillepich A., Glover S. C. O., Klessen R. S., 2022, *Monthly Notices of the Royal Astronomical Society*, **519**, 483
- Choi J., Dotter A., Conroy C., Cantiello M., Paxton B., Johnson B. D., 2016, *ApJ*, **823**, 102
- Ciardi D. R., Beichman C. A., Horch E. P., Howell S. B., 2015, *ApJ*, **805**, 16
- Claret A., 2017, *A&A*, **600**, A30
- Claret A., 2021, *Research Notes of the American Astronomical Society*, **5**, 13
- Cloutier R., et al., 2020, *AJ*, **160**, 22
- Cloutier R., et al., 2021, *AJ*, **162**, 79
- Cloutier R., et al., 2024, *MNRAS*, **527**, 5464
- Collins K. A., Kielkopf J. F., Stassun K. G., Hessman F. V., 2017, *AJ*, **153**, 77
- Cosentino R., et al., 2012, in McLean I. S., Ramsay S. K., Takami H., eds, *Society of Photo-Optical Instrumentation Engineers (SPIE) Conference Series* Vol. 8446, *Ground-based and Airborne Instrumentation for Astronomy IV*. p. 84461V, [doi:10.1117/12.925738](https://doi.org/10.1117/12.925738)
- Delrez L., et al., 2018, in Marshall H. K., Spyromilio J., eds, *Society of Photo-Optical Instrumentation Engineers (SPIE) Conference Series* Vol. 10700, *Ground-based and Airborne Telescopes VII*. p. 1070011 ([arXiv:1806.11205](https://arxiv.org/abs/1806.11205)), [doi:10.1117/12.2312475](https://doi.org/10.1117/12.2312475)
- Dressing C. D., Charbonneau D., 2015, *ApJ*, **807**, 45
- Dumusque X., et al., 2021, *Astronomy & Astrophysics*, **648**, A103
- Fűrész G., Szentgyorgyi A. H., Meibom S., 2008, in Santos N. C., Pasquini L., Correia A. C. M., Romaniello M., eds, *Precision Spectroscopy in Astrophysics*. pp 287–290, [doi:10.1007/978-3-540-75485-5_68](https://doi.org/10.1007/978-3-540-75485-5_68)
- Fairington T. R., et al., 2024, *MNRAS*, **527**, 8768
- Fausnaugh M. M., et al., 2021a, TESS Data Release Notes: Sector 42, DR60, https://archive.stsci.edu/missions/tess/doc/tess_drn/tess_sector_42_drn60_v02.pdf
- Fausnaugh M. M., et al., 2021b, TESS Data Release Notes: Sector 43, DR62, https://archive.stsci.edu/missions/tess/doc/tess_drn/tess_sector_43_drn62_v02.pdf
- Fausnaugh M. M., et al., 2022, TESS Data Release Notes: Sector 57, DR82, https://archive.stsci.edu/missions/tess/doc/tess_drn/tess_sector_57_drn82_v02.pdf
- Foley B. J., Driscoll P. E., 2016, *Geochemistry, Geophysics, Geosystems*, **17**, 1885
- Foreman-Mackey D., Hogg D. W., Lang D., Goodman J., 2013, *PASP*, **125**, 306
- Gaia Collaboration et al., 2023, *A&A*, **674**, A1
- Gan T., et al., 2020, *AJ*, **159**, 160
- García L. J., Timmermans M., Pozuelos F. J., Ducrot E., Gillon M., Delrez L., Wells R. D., Jehin E., 2021, *prose: FITS images processing pipeline*, *Astrophysics Source Code Library*, record ascl:2111.006 ([ascl:2111.006](https://ascl.net/2111.006))
- García L. J., Timmermans M., Pozuelos F. J., Ducrot E., Gillon M., Delrez L., Wells R. D., Jehin E., 2022, *MNRAS*, **509**, 4817
- Gardner J. P., et al., 2006, *Space Sci. Rev.*, **123**, 485
- Giacalone S., et al., 2021, *AJ*, **161**, 24
- Giclas H. L., Slaughter C. D., Burnham R., 1959, *Lowell Observatory Bulletin*, **4**, 136
- Giclas H. L., Burnham R., Thomas N. G., 1971, *Lowell proper motion survey Northern Hemisphere. The G numbered stars. 8991 stars fainter than magnitude 8 with motions > 0".26/year*. Lowell Observatory
- Gilbert E. A., et al., 2020, *AJ*, **160**, 116
- Gilbert E. A., et al., 2023, *ApJ*, **944**, L35
- Gillon M., 2018, *Nature Astronomy*, **2**, 344
- Gillon M., et al., 2017, *Nature*, **542**, 456
- Gliese W., 1956, *Z. Astrophys.*, **39**, 1
- Gliese W., 1969, *Veroeffentlichungen des Astronomischen Rechen-Instituts Heidelberg*, **22**, 1
- Guerrero N. M., et al., 2021, *ApJS*, **254**, 39
- Günther M. N., et al., 2019, *Nature Astronomy*, **3**, 1099
- Hojjatpanah S., et al., 2020, *A&A*, **639**, A35
- Howell S. B., Everett M. E., Sherry W., Horch E., Ciardi D. R., 2011, *AJ*, **142**, 19
- Hoyer S., Guterman P., Demangeon O., Sousa S. G., Deleuil M., Meunier J. C., Benz W., 2020, *A&A*, **635**, A24
- Ingersoll A. P., 1969, *Journal of Atmospheric Sciences*, **26**, 1191
- Irwin J., Berta Z. K., Burke C. J., Charbonneau D., Nutzman P., West A. A., Falco E. E., 2011, *ApJ*, **727**, 56
- Jehin E., et al., 2018, *The Messenger*, **174**, 2
- Jenkins J. M., 2002, *ApJ*, **575**, 493
- Jenkins J. M., et al., 2010, in Radziwill N. M., Bridger A., eds, *Society of Photo-Optical Instrumentation Engineers (SPIE) Conference Series* Vol. 7740, *Software and Cyberinfrastructure for Astronomy*. p. 77400D, [doi:10.1117/12.856764](https://doi.org/10.1117/12.856764)
- Jenkins J. M., et al., 2016, in Chiozzi G., Guzman J. C., eds, *Society of Photo-Optical Instrumentation Engineers (SPIE) Conference Series* Vol. 9913, *Software and Cyberinfrastructure for Astronomy IV*. p. 99133E, [doi:10.1117/12.2233418](https://doi.org/10.1117/12.2233418)
- Jenkins J. M., Tenenbaum P., Seader S., Burke C. J., McCauliff S. D., Smith J. C., Twicken J. D., Chandrasekaran H., 2020, *Kepler Data Processing Handbook: Transiting Planet Search*, *Kepler Science Document KSCI-19081-003*, id. 9. Edited by Jon M. Jenkins.
- Johnson D. R. H., Soderblom D. R., 1987, *AJ*, **93**, 864
- Kempton E. M. R., et al., 2018, *PASP*, **130**, 114401
- Kopparapu R. K., et al., 2013, *ApJ*, **765**, 131
- Kostov V. B., et al., 2019, *AJ*, **158**, 32
- Kreidberg L., 2015, *PASP*, **127**, 1161
- Kurucz R. L., 1992, in Barbuy B., Renzini A., eds, Vol. 149, *The Stellar Populations of Galaxies*. p. 225
- Lacedelli G., et al., 2022, *MNRAS*, **511**, 4551
- Lasker B. M., Sturch C. R., McLean B. J., Russell J. L., Jenkner H., Shara M. M., 1990, *AJ*, **99**, 2019
- Lépine S., Hilton E. J., Mann A. W., Wilde M., Rojas-Ayala B., Cruz K. L., Gaidos E., 2013, *AJ*, **145**, 102
- Li J., Tenenbaum P., Twicken J. D., Burke C. J., Jenkins J. M., Quintana E. V., Rowe J. F., Seader S. E., 2019, *PASP*, **131**, 024506
- Lim O., et al., 2023, *ApJ*, **955**, L22
- Lincowski A. P., Meadows V. S., Crisp D., Robinson T. D., Luger R., Lustig-Yaeger J., Arney G. N., 2018, *ApJ*, **867**, 76
- Luque R., et al., 2019, *A&A*, **628**, A39
- Lustig-Yaeger J., et al., 2023, *Nature Astronomy*, **7**, 1317
- Luyten W. J., 1976, *A catalogue of stars with proper motions exceeding 0".5 annually*. University of Minnesota
- Malavolta L., et al., 2016, *A&A*, **588**, A118
- Malavolta L., et al., 2018, *AJ*, **155**, 107
- Maldonado J., et al., 2020, *A&A*, **644**, A68

- Mandel K., Agol E., 2002, *ApJ*, **580**, L171
- Mann A. W., Feiden G. A., Gaidos E., Boyajian T., von Braun K., 2015, *ApJ*, **804**, 64
- Mann A. W., et al., 2019, *ApJ*, **871**, 63
- Maxted P. F. L., et al., 2022, *MNRAS*, **514**, 77
- May E. M., et al., 2023, *ApJ*, **959**, L9
- Medina A. A., Winters J. G., Irwin J. M., Charbonneau D., 2020, *ApJ*, **905**, 107
- Medina A. A., Winters J. G., Irwin J. M., Charbonneau D., 2022, *ApJ*, **935**, 104
- Ment K., Charbonneau D., 2023, *AJ*, **165**, 265
- Mignon L., et al., 2023, *A&A*, **675**, A168
- Moran S. E., et al., 2023, *ApJ*, **948**, L11
- Mortier A., Faria J. P., Correia C. M., Santerne A., Santos N. C., 2015, *A&A*, **573**, A101
- Mortier A., et al., 2020, *MNRAS*, **499**, 5004
- Muirhead P. S., et al., 2015, *ApJ*, **801**, 18
- Murray C. A., et al., 2020, *MNRAS*, **495**, 2446
- Nava C., López-Morales M., Haywood R. D., Giles H. A. C., 2020, *AJ*, **159**, 23
- Newton E. R., Charbonneau D., Irwin J., Berta-Thompson Z. K., Rojas-Ayala B., Covey K., Lloyd J. P., 2014, *AJ*, **147**, 20
- Newton E. R., Irwin J., Charbonneau D., Berta-Thompson Z. K., Dittmann J. A., West A. A., 2016, *ApJ*, **821**, 93
- Nordström B., et al., 2004, *A&A*, **418**, 989
- Otegi J. F., Bouchy F., Helled R., 2020, *A&A*, **634**, A43
- Owen J. E., Jackson A. P., 2012, *Monthly Notices of the Royal Astronomical Society*, **425**, 2931
- Owen J. E., Murray-Clay R., 2018, *Monthly Notices of the Royal Astronomical Society*, **480**, 2206
- Palethorpe L., et al., 2024, *MNRAS*, **529**, 3323
- Patel J. A., Espinoza N., 2022, *AJ*, **163**, 228
- Pierrehumbert R. T., Hammond M., 2019, *Annual Review of Fluid Mechanics*, **51**, 275
- Rackham B. V., Apai D., Giampapa M. S., 2018, *ApJ*, **853**, 122
- Ricker G., 2021, in 43rd COSPAR Scientific Assembly. Held 28 January - 4 February. p. 499
- Ricker G. R., et al., 2014, in Oschmann Jacobus M. J., Clampin M., Fazio G. G., MacEwen H. A., eds, *Society of Photo-Optical Instrumentation Engineers (SPIE) Conference Series Vol. 9143, Space Telescopes and Instrumentation 2014: Optical, Infrared, and Millimeter Wave*. p. 914320 ([arXiv:1406.0151](https://arxiv.org/abs/1406.0151)), doi:10.1117/12.2063489
- Rieke G. H., et al., 2015, *PASP*, **127**, 584
- Rodríguez J. E., et al., 2020, *AJ*, **160**, 117
- Schönrich R., Binney J., Dehnen W., 2010, *MNRAS*, **403**, 1829
- Scott N. J., Howell S. B., Horch E. P., Everett M. E., 2018, *PASP*, **130**, 054502
- Seager S., Deming D., 2010, *ARA&A*, **48**, 631
- Sebastian D., et al., 2021, *A&A*, **645**, A100
- Shporer A., et al., 2020, *ApJ*, **890**, L7
- Silverstein M. L., et al., 2022, *AJ*, **163**, 151
- Skrutskie M. F., et al., 2006, *AJ*, **131**, 1163
- Smith J. C., et al., 2012, *PASP*, **124**, 1000
- Soubiran C., et al., 2018, *A&A*, **616**, A7
- Speagle J. S., 2020, *MNRAS*, **493**, 3132
- Stassun K. G., et al., 2019, *AJ*, **158**, 138
- Stumpe M. C., et al., 2012, *PASP*, **124**, 985
- Stumpe M. C., Smith J. C., Catanzarite J. H., Van Cleve J. E., Jenkins J. M., Twicken J. D., Girouard F. R., 2014, *PASP*, **126**, 100
- Suárez Mascareño A., Rebolo R., González Hernández J. I., Esposito M., 2015, *MNRAS*, **452**, 2745
- Suárez Mascareño A., et al., 2018, *A&A*, **612**, A89
- Suissa G., et al., 2020, *AJ*, **160**, 118
- Trifonov T., et al., 2021, *Science*, **371**, 1038
- Tuson A., et al., 2023, *MNRAS*, **523**, 3090
- Twicken J. D., et al., 2018, *PASP*, **130**, 064502
- Vanderspek R., et al., 2019, *ApJ*, **871**, L24
- Veyette M. J., Muirhead P. S., 2018, *ApJ*, **863**, 166
- Vines J. I., Jenkins J. S., 2022, *MNRAS*, **513**, 2719
- Wilson T. G., et al., 2022, *MNRAS*, **511**, 1043
- Winters J. G., et al., 2019, *AJ*, **158**, 152
- Winters J. G., Charbonneau D., Henry T. J., Irwin J. M., Jao W.-C., Riedel A. R., Slatten K., 2021, *AJ*, **161**, 63
- Wizinowich P., et al., 2000, *PASP*, **112**, 315
- Wunderlich F., et al., 2019, *A&A*, **624**, A49
- Zahnle K. J., Catling D. C., 2017, *ApJ*, **843**, 122
- Zieba S., et al., 2023, *Nature*, **620**, 746

AFFILIATIONS

¹University of Southern Queensland, Centre for Astrophysics, West Street, Toowoomba, QLD 4350 Australia

²SUPA, Institute for Astronomy, University of Edinburgh, Blackford Hill, Edinburgh, EH9 3HJ, UK

³Centre for Exoplanet Science, University of Edinburgh, Edinburgh, EH9 3HJ, UK

⁴Mullard Space Science Laboratory, University College London, Holmbury St Mary, Dorking, Surrey, RH5 6NT, UK

⁵School of Physics and Astronomy, University of Birmingham, Edgbaston, Birmingham B15 2TT, UK

⁶Department of Physics, University of Warwick, Gibbet Hill Road, Coventry CV4 7AL, UK

⁷Centre for Exoplanets and Habitability, University of Warwick, Coventry, CV4 7AL, UK

⁸Fundación Galileo Galilei - INAF (Telescopio Nazionale Galileo), Rambla José Ana Fernández Pérez 7, E-38712 Breña Baja (La Palma), Canary Islands, Spain

⁹Instituto de Astrofísica de Canarias, C/Vía Láctea s/n, E-38205 La Laguna (Tenerife), Canary Islands, Spain

¹⁰Departamento de Astrofísica, Univ. de La Laguna, Av. del Astrofísico Francisco Sánchez s/n, E-38205 La Laguna (Tenerife), Canary Islands, Spain

¹¹NASA Exoplanet Science Institute, IPAC, California Institute of Technology, Pasadena, CA 91125 USA

¹²Department of Physics & Astronomy, McMaster University, 1280 Main St W, Hamilton, ON, L8S 4L8, Canada

¹³Astrobiology Research Unit, University of Liège, Allée du 6 août, 19, 4000 Liège (Sart-Tilman), Belgium

¹⁴Space Sciences, Technologies and Astrophysics Research (STAR) Institute, Université de Liège, Allée du 6 Août 19C, 4000 Liège, Belgium

¹⁵Institute of Astronomy, KU Leuven, Celestijnenlaan 200D, 3001 Leuven, Belgium

¹⁶AIM, CEA, CNRS, Université Paris-Saclay, Université de Paris, F-91191 Gif-sur-Yvette, France

¹⁷Department of Physics and Astronomy, The University of New Mexico, 210 Yale Blvd NE, Albuquerque, NM 87106, USA

¹⁸NSF's National Optical-Infrared Astronomy Research Laboratory, 950 N. Cherry Ave., Tucson, AZ 85719, USA

¹⁹Astrobiology Research Unit, Université de Liège, Allée du 6 Août 19C, 4000 Liège, Belgium

²⁰Cavendish Laboratory, JJ Thomson Avenue, Cambridge CB3 0HE, UK

²¹Department of Physics and Kavli Institute for Astrophysics and Space Research, Massachusetts Institute of Technology, Cambridge, MA 02139, USA

²²Juan Carlos Torres Fellow

²³Center for Astrophysics | Harvard & Smithsonian, 60 Garden St, Cambridge, MA 02138, USA

²⁴CAS Key Laboratory of Planetary Sciences, Purple Mountain Observatory, Chinese Academy of Sciences, Nanjing 210008, China

²⁵Proto-Logic Consulting LLC, Washington, DC

²⁶Department of Astrophysical and Planetary Sciences, University of Colorado Boulder, Boulder, CO 80309, USA

²⁷Department of Earth, Atmospheric and Planetary Sciences, Massachusetts Institute of Technology, Cambridge, MA 02139, USA

²⁸Department of Aeronautics and Astronautics, MIT, 77 Massachusetts Avenue, Cambridge, MA 02139, USA

APPENDIX A: RV DATA

Table A1. TRES radial velocity data and activity indicators.

BJD _{UTC} (d)	RV (m s ⁻¹)	σ_{RV} (m s ⁻¹)	pha	Teff	σ_{Teff}	Vrot	σ_{Vrot}	CCF	SNRe
2457674.500000	51286	21	-71.41	0.0	0.0	0.0	0.5	0.931	20.1
2457920.500000	51308	21	-61.76	0.0	0.0	0.8	0.5	0.940	23.5
2458654.500000	51279	21	-33.00	0.0	0.0	1.9	0.5	0.915	16.2
2459468.500000	51256	21	-1.11	0.0	0.0	1.5	0.5	0.947	23.3

Table A2. HARPS-N radial velocity data and activity indicators.

BJD _{UTC} (d)	RV (CCF) (m s ⁻¹)	σ_{RV} (CCF) (m s ⁻¹)	RV (LBL) (m s ⁻¹)	σ_{RV} (LBL) (m s ⁻¹)	BIS _{span} (m s ⁻¹)	$\sigma_{BIS_{span}}$ (m s ⁻¹)	FWHM (km s ⁻¹)	σ_{FWHM} (km s ⁻¹)	H α	$\sigma_{H\alpha}$	S-index	$\sigma_{S-index}$	$\log R'_{HK}$	$\sigma_{\log R'_{HK}}$
2460165.657371	51336.09	2.48	51067.47	0.91	1932.44	4.96	2.65965	0.00496	0.639720	0.000441	0.803612	0.015745	-5.706724	0.012155
2460166.649562	51337.54	6.53	51069.37	2.02	2133.89	13.06	2.67660	0.01306	0.624102	0.001419	0.624944	0.068003	-5.872690	0.076935
2460171.600859	51338.04	3.02	51070.06	1.14	1949.39	6.04	2.65876	0.00604	0.672546	0.000691	0.891012	0.024193	-5.644005	0.016166
2460172.701740	51330.58	2.36	51065.07	0.95	2001.89	4.72	2.66160	0.00472	0.640433	0.000522	0.844017	0.015760	-5.676600	0.011352
2460173.618065	51335.21	2.21	51067.12	0.94	1885.06	4.42	2.65677	0.00441	0.663422	0.000570	0.841318	0.015271	-5.678549	0.011049
2460174.667788	51334.79	2.24	51065.35	0.94	1914.42	4.47	2.66415	0.00447	0.649150	0.000555	0.899625	0.014965	-5.638287	0.009869
2460193.607987	51338.87	2.42	51071.24	0.97	1914.82	4.85	2.66358	0.00485	0.665288	0.000552	0.886741	0.016841	-5.646868	0.011328
2460196.589712	51337.73	2.64	51070.34	1.20	1958.99	5.27	2.66226	0.00527	0.869402	0.001124	1.526949	0.024313	-5.347680	0.008211
2460198.605434	51338.94	3.10	51072.07	1.38	2006.43	6.21	2.66566	0.00621	0.682733	0.001251	0.780828	0.026873	-5.724680	0.021622
2460199.632412	51339.12	1.89	51070.26	0.83	1957.92	3.77	2.66797	0.00377	0.625008	0.000478	0.859892	0.011799	-5.665314	0.008281
2460208.578168	51338.38	2.97	51068.59	1.16	1926.13	5.93	2.66443	0.00593	0.635852	0.000746	0.889042	0.023664	-5.645323	0.015860
2460215.542502	51341.32	3.86	51076.16	1.69	1812.75	7.73	2.65975	0.00773	0.631869	0.001897	0.714995	0.034402	-5.781169	0.031525
2460218.560370	51339.23	3.73	51071.97	1.46	1956.52	7.46	2.65768	0.00746	0.602605	0.001217	0.662081	0.034328	-5.832585	0.035411

APPENDIX B: ADDITIONAL FIGURES

This paper has been typeset from a \TeX/L\AA\TeX file prepared by the author.

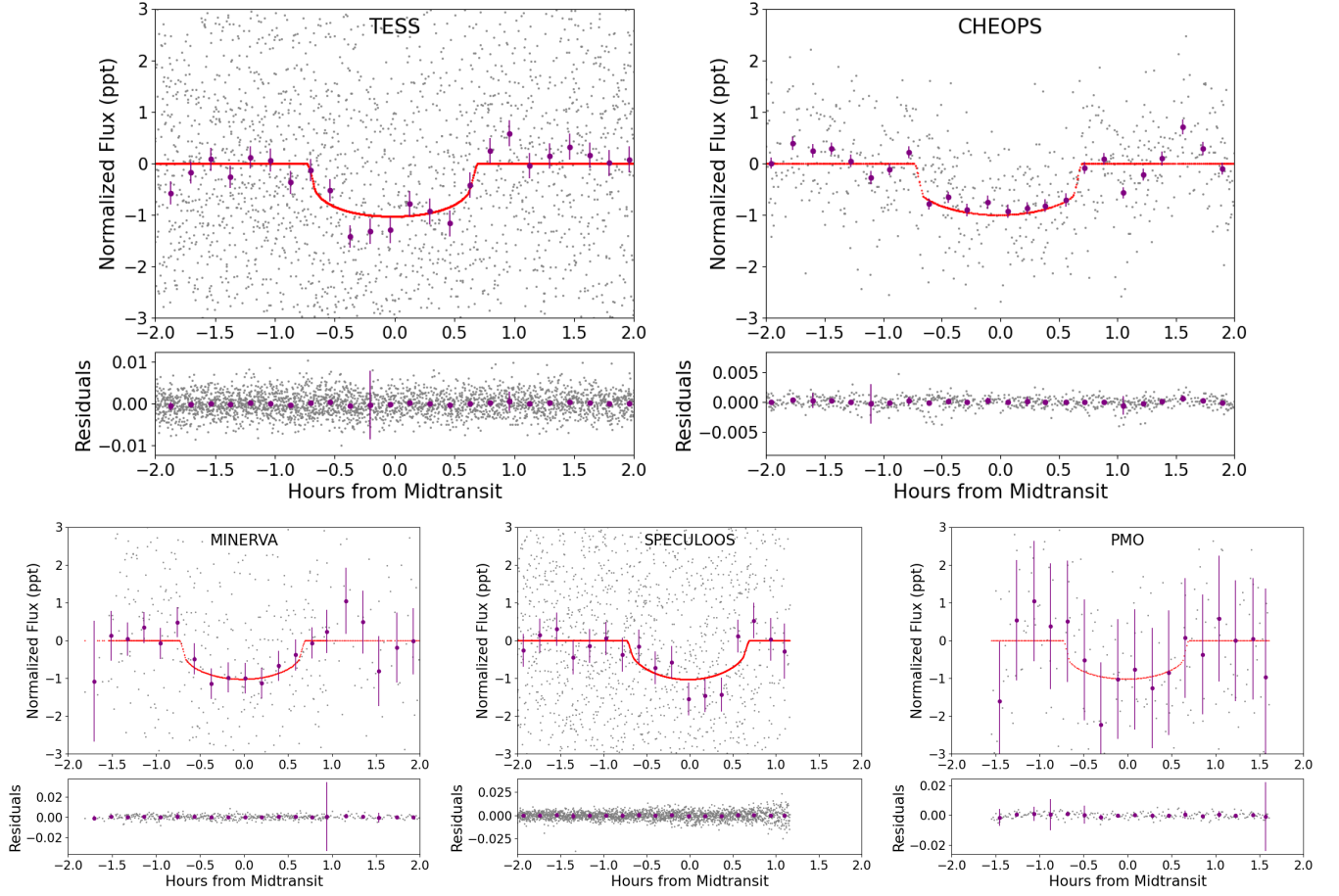


Figure B1. Phased transits of Gliese 12 b from fit results obtained with *dynesty*. Transit fit to the light curve data from *TESS* (top left), *CHEOPS* (top right), *MINERVA* (bottom left), *SPECULOOS* (bottom), and *PMO* (bottom right). The short cadence (20s for *TESS* sectors 42, 43, and 57, 120s for *TESS* sector 70, 30s for *CHEOPS*, 10s for all *SPECULOOS* telescopes, 30s for *MINERVA* T1, 60s for *MINERVA* T2, and 55s for *PMO*) fluxes are plotted in grey, the binned fluxes are overplotted in purple (10 minutes for space-based data and 11.5 minutes for ground-based data), and the fitted transit is shown by the red solid line.